

JGR Solid Earth

L

RESEARCH ARTICLE

10.1029/2025JB031367

Key Points:

- We present an algorithm that uses Kirchhoff migration with diffracted S-waves to detect heterogeneities at the base of the mantle
- High-frequency hybrid simulations show the method is most effective when applied using multiple earthquakes
- We successfully apply this approach to real data, detecting ultralow velocity zone structures with varying lateral dimensions

Supporting Information:

Supporting Information may be found in the online version of this article.

Correspondence to:

J. Wolf, wolf@ucsc.edu

Citation:

Wolf, J., Garnero, E., Schwarz, B., Leng, K., Luo, Y., Maass, R., & West, J. D. (2025). Detection of lowermost mantle heterogeneity using seismic migration of diffracted S-waves. *Journal of Geophysical Research: Solid Earth, 130*, e2025JB031367. https://doi.org/10.1029/2025JB031367

Received 14 FEB 2025 Accepted 22 MAY 2025

Author Contributions:

Edward Garnero

Data curation: John D. West

Formal analysis: Jonathan Wolf

Funding acquisition: Jonathan Wolf,

Edward Garnero

Investigation: Jonathan Wolf,

Benjamin Schwarz, Kuangdai Leng

Methodology: Jonathan Wolf,

Edward Garnero, Benjamin Schwarz,

Conceptualization: Jonathan Wolf,

Regina Maass **Project administration:** Jonathan Wolf

© 2025. The Author(s).

Kuangdai Leng, Yantao Luo,

This is an open access article under the terms of the Creative Commons
Attribution-NonCommercial-NoDerivs
License, which permits use and
distribution in any medium, provided the original work is properly cited, the use is non-commercial and no modifications or adaptations are made.

Detection of Lowermost Mantle Heterogeneity Using Seismic Migration of Diffracted S-Waves

Jonathan Wolf^{1,2,3} , Edward Garnero⁴, Benjamin Schwarz⁵ , Kuangdai Leng⁶ , Yantao Luo⁷ , Regina Maass⁸ , and John D. West⁴

¹Department of Earth and Planetary Science, University of California, Berkeley, CA, USA, ²Miller Institute for Basic Research in Science, Berkeley, CA, USA, ³Department of Earth and Planetary Sciences, University of California, Santa Cruz, CA, USA, ⁴School of Earth and Space Exploration, Arizona State University, Tempe, AZ, USA, ⁵Fraunhofer Institute for Wind Energy Systems IWES, Bremerhaven, Germany, ⁶Rutherford Appleton Laboratory, Science and Technology Facilities Council, Didcot, UK, ⁷SLB, Houston, TX, USA, ⁸Geophysics Section, Dublin Institute for Advanced Studies, Dublin, Ireland

Abstract The bottom of Earth's mantle hosts strong seismic wave speed heterogeneities. These are commonly detected via forward modeling of seismic waveforms, which can include time-consuming waveform synthesis and visual inspection. Furthermore, such imaging has been most commonly carried out with waves that have limited global coverage. In this work, we investigate the efficacy of the diffracted $S(S_{diff})$ wavefield, which has global coverage to map core-mantle boundary heterogeneity. We implement a Kirchhoff migration algorithm to objectively investigate the presence or absence of postcursors to S_{diff} , caused by ultralow velocity zones (ULVZs) and other sharp velocity contrasts. Our approach makes use of the expected moveout of ULVZgenerated S_{diff} postcursors as a function of distance from great-circle path at the base of the mantle. We investigate epicentral distances $>95^{\circ}$, where S_{diff} includes asymptotic S/ScS up to diffraction. We test the algorithm using synthetic waveforms calculated for models that include lowermost mantle wavespeed heterogeneity via a recently proposed hybrid simulation approach. Our results demonstrate that the migration approach, when applied to a single event, can well resolve the location of heterogeneity structures in the azimuthal direction, but is less accurate at constraining the along-great circle path location. To locate ULVZ structure accurately, heterogeneity maps from different earthquakes with crisscrossing raypaths are combined. Lastly, we provide real-data proof-of-concept examples which detect ULVZs with different sizes that have been proposed in past work. These include the Hawaiian ULVZ, which is roughly 1,000 km across and a ULVZ beneath the Himalayas with a lateral extent of only 200 km.

Plain Language Summary Low-velocity heterogeneity at the base of the mantle can be detected using seismic waves from distant earthquakes that travel horizontally along the core-mantle boundary (CMB). When these waves interact with CMB heterogeneity, they can be scattered in all directions. Here, we employ a method that assumes that every point on the CMB is a potential scattering location of seismic waves, and predicts arrival times of the scattered energy from every point. Seismic energy from multiple sensors is summed according to time predictions from each scatterer location. Stacked waveforms having high energy indicate the location of a likely scatterer. This process is called Kirchhoff migration. We employ a computer algorithm to search for locations of heterogeneous structures using computer-calculated (synthetic) data. These tests reveal that the algorithm can locate heterogeneity with different accuracies depending on where it is positioned relative to the seismic source and receivers. We then apply our migration procedure to real seismic recordings and demonstrate that we can reproduce results from previous studies.

1. Introduction

Earth's lowermost mantle hosts strong seismic wave speed heterogeneities across a wide range of spatial scales (e.g., McNamara, 2019; Tkalčić et al., 2015; Yu & Garnero, 2018). The most prominent deep mantle features are the two antipodal provinces with seismic velocities that are reduced by a few percent compared to the depth-average, the large-low velocity provinces (LLVPs) (e.g., Dziewonski et al., 1977; Garnero et al., 2016; Lekic et al., 2012). Their properties and origin are currently not precisely understood (e.g., McNamara, 2019). Much smaller anomalies with more extreme velocity anomalies, located in the 10's of km at the base of the mantle atop the core-mantle boundary (CMB), are called ultra-low velocity zones (ULVZs). These may be made of (partially)

WOLF ET AL. 1 of 19



Journal of Geophysical Research: Solid Earth

10.1029/2025JB031367

Resources: Jonathan Wolf,
Edward Garnero
Software: Jonathan Wolf, Kuangdai Leng
Validation: Jonathan Wolf
Visualization: Jonathan Wolf,
Edward Garnero, Kuangdai Leng
Writing – original draft: Jonathan Wolf
Writing – review & editing:
Jonathan Wolf, Edward Garnero,
Benjamin Schwarz, Kuangdai Leng,
Yantao Luo, Regina Maass, John D. West

molten materials (e.g., Simmons & Grand, 2002; Thorne et al., 2019; Williams & Garnero, 1996; Yuan & Romanowicz, 2017), or solid iron-rich material of unknown origin (e.g., Dobrosavljevic et al., 2019; Dobrosavljevic et al., 2023; Lai et al., 2022), and their presence has been explained by a variety of different mechanisms (see Yu & Garnero, 2018). Furthermore, there is evidence for heterogeneities with spatial dimensions of a few kilometers (Frost et al., 2017; Ma & Thomas, 2020; Tkalčić et al., 2015) in the lowermost mantle, whose properties are currently challenging to analyze in detail due to the small wavelengths needed to investigate them.

ULVZs have been mapped with lateral dimensions of 100's of km across, and exhibit seismic velocity reductions of several tens of percent compared to standard reference Earth models (e.g., McNamara, 2019; Yu & Garnero, 2018). ULVZs have been detected using different seismic phases (e.g., Avants et al., 2006; Cottaar & Romanowicz, 2012; Garnero et al., 1993; Li et al., 2022; Thorne et al., 2021). For example, they can cause (relative) delay times of waves traveling through the structure (e.g., Festin et al., 2024; Garnero et al., 1993; Thorne et al., 2021; Wolf, Li, & Long, 2024), as well as pre- and postcursors (e.g., Cottaar & Romanowicz, 2012; Hansen et al., 2023; Jenkins et al., 2021; Yuan & Romanowicz, 2017) of seismic waves, which can be exploited for their detection. Large or mega-ULVZs (ULVZs \sim 500–1,000 km across) have been detected and characterized using postcursors (Figure 1b) of $S_{\rm diff}$ waves (e.g., Cottaar & Romanowicz, 2012; Martin et al., 2023; Yuan & Romanowicz, 2017), which are shear waves that diffract along the CMB (Figure 1c). Such procedures can also be applied to the combined S/ScS phase (Figure 1) down to pre-diffraction epicentral distances of 95° (e.g., Wolf & Long, 2023). The combined S/ScS and $S_{\rm diff}$ phases, when analyzed as a function of event azimuth, are sometimes referred to as S* (Wolf & Long, 2023).

A commonly employed method for seismic investigation of subsurface heterogeneities involves dividing the study area into a grid and considering each grid point as a potential scatterer location. For each potential scatterer, the arrival times of the scattered wave at all stations are estimated, which follow a close-to-hyperbolic trajectory in seismic record section plots. The scattered energy across stations can then be stacked along the predicted travel times to give an estimate of the scattering potential at any given grid location. This process, called seismic migration (e.g., Etgen et al., 2009), is frequently applied to image the shallow Earth (e.g., Gazdag & Sguazzero, 1984; Gray et al., 2001; Landa et al., 1987; Schwarz, 2019a), but has also been utilized to image both the upper (e.g., Bostock & Rondenay, 1999; Luo et al., 2022, 2025; Rondenay, 2009) and the lowermost (e.g., Hutko et al., 2006; Lay & Young, 1996; Thomas et al., 2004) mantle. Typically, migration approaches are used to image topographies of interfaces. In these cases, seismic wave scattering is, in fact, caused by large contiguous structures, and migration results may not clearly identify them as such (e.g., Lay & Young, 1996; Thomas et al., 2004). Single scatterers (e.g., Niu et al., 2004) as well as likely scattering volumes (e.g., Hedlin & Shearer, 2000) have also been imaged. Single scatterers cause seismic arrivals with approximately hyperbolic moveout as a function of lateral distance in near-surface imaging (e.g., Schwarz, 2019a), which appear visually similar to postcursors of S* caused by ULVZs (Figure 1). Strictly speaking, S* postcursors are due to more complex effects such as refraction inside the ULVZ (e.g., Cottaar & Romanowicz, 2012; Li et al., 2022; Martin et al., 2023) and not due to a single scattering instance. However, Figure 1 suggests that, at sufficiently large periods (>4 s), the kinematics of postcursors caused by ULVZ structure can increasingly be governed by assuming the presence of a single scatterer located at the center of the ULVZ.

In this study, we implement a migration approach and estimate the location of lowermost mantle heterogeneity using S*. While the identified CMB anomalies may often be ULVZs, our method does not constrain the precise properties of the scatterers, as full-wave simulations do to some extent. The central advantage of our proposed methodology is that it is fast, taking \sim 1 min per event using one core-processing unit, which is \sim 10⁶ times faster than full-wave simulations. S* waves (especially S_{diff}) achieve a global coverage along the CMB. Thus, this method holds promise for identifying ULVZ structure globally.

2. High-Frequency Hybrid Waveform Simulations

We calculate synthetic seismograms for lowermost mantle heterogeneity signals to test how well we can retrieve them using a Kirchhoff migration method. For these simulations, we often use the event coordinates (179.92° East, 23.78° South) of an event that occurred on 29 July 2011, near Fiji. For simplicity, we assume an event depth of 0 km and a focal mechanism that maximizes (horizontally polarized) SH energy. We use this event location because an event at the same location has been used in a previous ULVZ analysis (Wolf & Long, 2023), thus permitting a direct comparison. Whenever we compute synthetic seismograms for other event locations, we rotate

WOLF ET AL. 2 of 19

21699356, 2025, 6, Downloaded from https://agupubs.onlinelibrary.wiley.com/doi/10.1029/2025JB031367 by Ingv, Wiley Online Library on [11/11/2025]. See the Terms and Conditions (https://onlinelibrary.wiley.com/doi/10.1029/2025JB031367 by Ingv, Wiley Online Library on [11/11/2025]. See the Terms and Conditions (https://onlinelibrary.wiley.com/doi/10.1029/2025JB031367 by Ingv, Wiley Online Library on [11/11/2025]. See the Terms and Conditions (https://onlinelibrary.wiley.com/doi/10.1029/2025JB031367 by Ingv, Wiley Online Library on [11/11/2025]. See the Terms and Conditions (https://onlinelibrary.wiley.com/doi/10.1029/2025JB031367 by Ingv, Wiley Online Library on [11/11/2025]. See the Terms and Conditions (https://onlinelibrary.wiley.com/doi/10.1029/2025JB031367 by Ingv, Wiley Online Library on [11/11/2025]. See the Terms and Conditions (https://onlinelibrary.wiley.com/doi/10.1029/2025JB031367 by Ingv, Wiley Online Library on [11/11/2025].

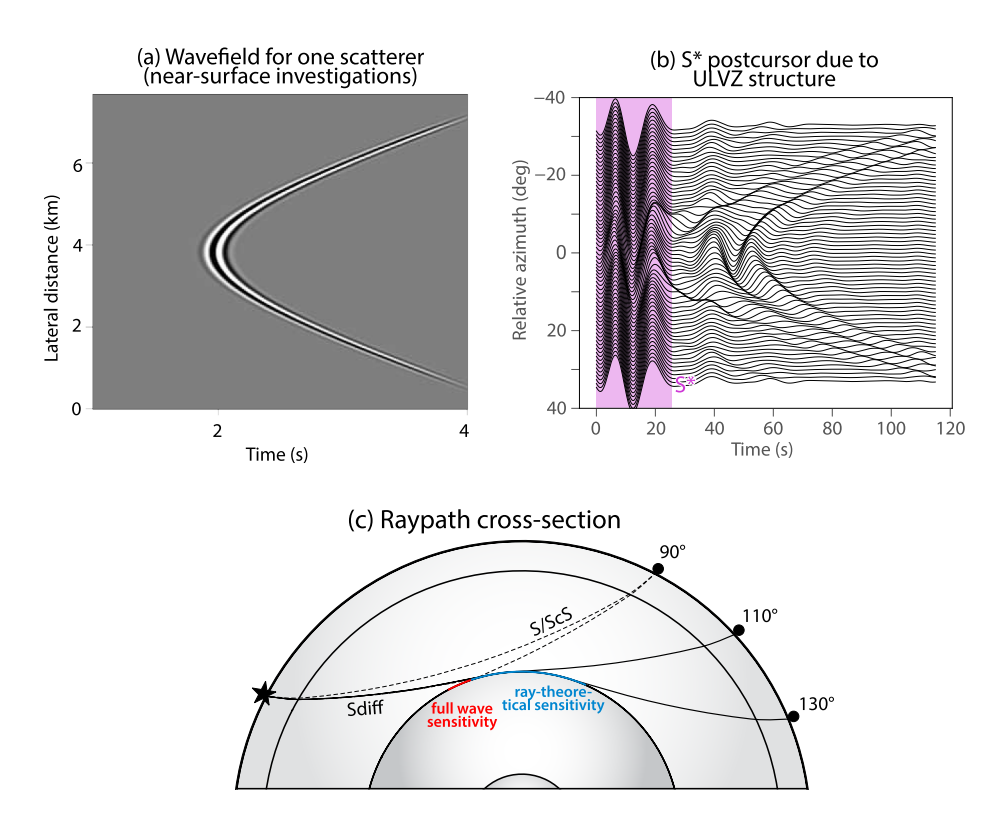


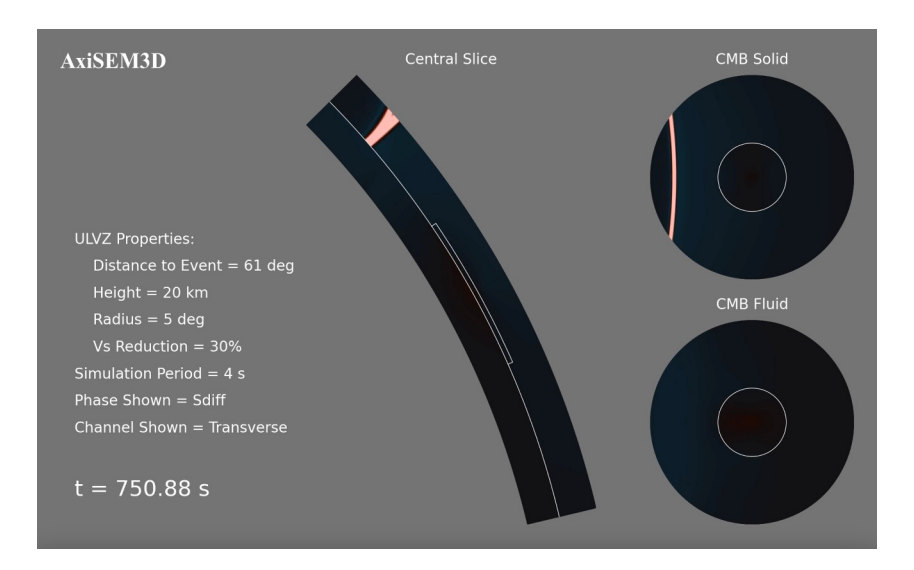
Figure 1. (a) Example wavefield caused by a single scatterer, as experienced in near-surface seismics (Schwarz, 2019a). (b) Synthetic transverse displacement seismograms around and after the predicted S* arrival (pink shading), calculated for an Earth model that includes a ultralow velocity zone (5° radius, 61° distance from event) and stations at 110° distance. S* postcursors with a hyperbolic time moveout as a function of azimuth are visible. These postcursors are similar to the scattered wavefield in panel (a), although their length and timescales differ. (c) Cross-section of S, ScS (dashed lines), and S_{diff} (solid lines) raypaths through Earth's mantle, which we refer to as S*. The source is depicted as a black star and the stations as black circles. The area of ray-theoretical core-mantle boundary sensitivity for these seismic waves is highlighted in light blue. Full-wave sensitivity extends beyond this area at both slightly lower (red) and larger distances. For the approach in this paper, only the implementation for lower distances important (see text).

the moment tensor such that the source polarization relative to the ULVZ stays the same for comparability. The source-receiver setup for our synthetic tests using the Fiji event is presented in Figure 3a. Stations are placed at epicentral distances between 95° and 120° and at azimuths within $\pm 40^{\circ}$ relative to its central azimuth (Figure 3a). Distance and azimuth intervals at which we place stations are both 1° .

We compute 3D full wave synthetics down to a period of 4 s, incorporating PREM (Dziewonski & Anderson, 1981) velocities in the mantle, with lowermost mantle heterogeneity and PREM-attenuation. We implement a hybrid modeling framework (Leng et al., 2020) that decomposes the total wavefield into an incident and a scattered part (due to heterogeneity) using the modeling code AxiSEM3D (Leng et al., 2016, 2019). This is efficient due to the low azimuthal complexity of the incident and scattered part of the wavefield respectively in the source- and ULVZ-centered coordinate frames, which can be solved exactly in two sequential simulations (Leng et al., 2020). We conduct simulations for a cylindrical 20 km high ULVZ. This shape is motivated by that put forth in previous ULVZ studies using S_{diff} (e.g., Cottaar & Romanowicz, 2012; Li et al., 2022), although differently shaped ULVZ heterogeneities lead to similar waveform effects. Unless stated differently, we assume a shear velocity reduction of 30% and a P velocity reduction of 10% (one-third of the S reduction, in alignment with the melt hypothesis for ULVZ origin, e.g., Williams and Garnero (1996)). We note that there is significant tradeoff between ULVZ velocity and thickness (Festin et al., 2024; Jenkins et al., 2021; Lai et al., 2022; Vanacore et al., 2016); these also exist for S* postcursors (e.g., Cottaar & Romanowicz, 2012; Martin et al., 2023; Wolf & Long, 2023). We implement ULVZs that are 10° across (roughly 650 km at the CMB), placed at different epicentral distances from the source (Figure 3a) to test how migration results change depending on the along-great circle position of the ULVZ. We additionally implement different lateral ULVZ dimensions (diameters of 4°, 10°, and 16°) for an epicentral distance of 60° from the source. Since sharp edges with a few percent velocity contrast,

WOLF ET AL. 3 of 19

21699356, 2025. 6, Downloaded from https://agupubs.onlinelibrary.wiley.com/doi/10.1029/2025JB031367 by Ingv, Wiley Online Library on [11/11/2025]. See the Terms and Conditions



Animation 1. Animation of seismic wave propagation through ULVZ structure for a cylindrical ULVZ with a height of 20 km, a radius of 5° , a velocity reduction of 30% placed at a source distance of 61° . Displacement in SH-direction is shown from three different angles: The central slice through the ULVZ, and, looking from above, solid and fluid displacement at CMB. In the projections to the right, the outline of the ULVZ is represented as the inner white circle. Multiple postcursors are produced after the main S_{diff} pulse (incoming wavefront). A quasi-hyperbolic postcursor is radiated to a large range of directions with a relatively large amplitude (CMB Solid). The fluid displacements are P waves generated by the ULVZ, which is non-zero in the SH direction in reference to the earthquake.

as observed at LLVP boundaries, have been shown to cause postcursors similar to ULVZs (e.g., Ni et al., 2005; To et al., 2005), we also implement such sharp edges across which both shear and P velocity contrasts are 3%.

Animation 1 shows SH wave propagation through a cylindrical ULVZ located 61° from the source, illuminating how quasi-hyperbolic postcursors are produced. As the wavefront hits the edge of the ULVZ, it gets distorted: Some energy travels at the speeds of the mantle above the ULVZ and other energy at the speeds within the ULVZ, accumulating a relative delay. This leads to complex wavefield effects for energy traveling through the ULVZ at azimuths close to the great circle path. Strictly speaking, more than one postcursor is produced, two of which have a simple geometric explanation: One postcursor is caused by energy diffracting around the edge of the ULVZ and a second postcursor by refraction within the ULVZ, the latter of which has a larger amplitude. This postcursor shows a quasi-hyperbolic moveout and will be exploited in the approach that is described in the following.

3. Travel Time Calculations for a Potential Scatterer

We predict arrival times for energy scattered at a particular CMB location (Figure 2a). Specifically, we are interested in the differential travel time between the main S* wave and the postcursor caused by the scatterer (e.g., between the paths depicted in Figure 2a). For this calculation we use Pyekfmm (Chen et al., 2023), which efficiently solves the eikonal equation in either two or three dimensions via the fast marching method (Sethian, 1996). We assume PREM (Dziewonski & Anderson, 1981) velocities along the CMB and do not consider 3D velocity heterogeneity in our computation of postcursor travel times. This might result in small scatterer location errors, but does not affect our ability to detect heterogeneity.

Pyekfmm uses spherical coordinates, enabling us to conduct our calculations only for a reduced latitude and longitude range (and not the whole globe) if the reference frame is rotated. We implement a rotation such that the seismic event is at the south pole (Figure 3a), ensuring higher computational efficiency. As a result, our grid has a regular azimuth-distance sampling, but causes the bins to vary slightly in area. However, this is the most natural implementation because the waveform analysis (described in Section 5.3) is conducted for varying azimuth. This rotation is displayed in Figure 3 for the Fiji event.

For each potential scatterer location defined by the CMB migration grid, the travel time from source to scatterer is calculated using Pyekfmm ($T_{source-scatterer}$). Then, we determine the travel times from the scatterer to each

WOLF ET AL. 4 of 19



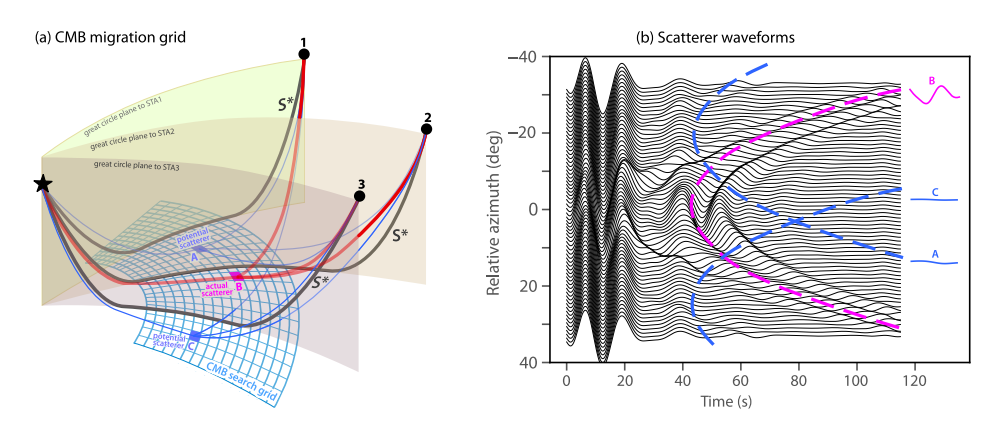


Figure 2. Schematic representation of Kirchhoff migration scheme. (a) Great-circle raypaths from source (black star) to receivers (black circles) are shown as black lines. A grid of potential scatterers (light blue) is implemented at the core-mantle boundary. Raypaths from source to potential scatterers (blue and pink), and then to the station, are shown by red (dashed and solid) red lines. Only scatterer B (pink) marks an actual scatterer location. (b) Transverse S* displacement waveforms as a function of azimuth (black). Waveforms are stacked along predicted scatterer postcursor arrival times (blue and pink dashed lines), and stacked waveforms are shown to the right. Only for the actual scatterer B (pink hyperbola) does the stacked waveform have a high amplitude (right). These waveforms are for a ultralow velocity zone that is 4° across and stations at 103° source-receiver distance.

receiver ($T_{scatterer-receiver}$), as well as the direct S* wave from source to receiver ($T_{source-receiver}$). For each scatterer and station, the delay time of a potential postcursor can then be expressed as

$$T_{delay} = T_{source-scatterer} + T_{scatterer-receiver} - T_{source-receiver}. \tag{1}$$

4. Postcursor Properties and the Scatterer Assumption

The precise delay time of the S* postcursor relative to the main arrival depends on several factors. These include the epicentral distance between the source and receiver, the detailed characteristics of the ULVZ, such as its size and velocity reduction, and the frequency content of the data being analyzed. For instance, as the epicentral distance grows, the postcursor moveout broadens as a function of azimuth (Figure 4a). From here on, we refer to this shape as the postcursor convexity (Figure 4d). Changing the ULVZ size, on the other hand, mainly affects the minimum postcursor delay time relative to S* (Figures 4b and 4d). In our case, postcursor delay times are only weakly dependent on frequency (Figure 4c), but this dependence would be stronger for even thinner velocity structures (Li et al., 2022).

Figures 4a–4c also show predicted postcursor arrival times for a scatterer at the CMB, located at the ULVZ mid point (Section 3). Naturally, the predicted minimum delay time for a scatterer relative to S* is 0 s, which is unlike what is observed for ULVZs. However, the predicted postcursor convexity is very similar to what is observed for postcursors due to ULVZ structure (Figures 4a–4c). If the minimum delay time relative to S* and the postcursor convexity (Figure 4d) are adjusted, the postcursor response caused by ULVZ structure can be approximated using the single scatterer assumption (Figure 4d). Therefore, despite substantial wavefield complexities caused by ULVZ structure (Animation 1), scatterer predictions can help describe the most significant arrivals after S* that are caused by ULVZ structure.

5. Kirchhoff Migration Method

5.1. Overview

As described earlier, Kirchhhoff migration is a method that involves computation of travel times between locations of points on a grid in a sub-surface region of interest to all events and stations. These are used to sum (or stack) waveform data to image potential reflections (or scatterers) at all grid points. It thus permits construction of a visual representation of, in our case, plausible CMB locations of scatterering heterogeneity. The following subsections describe aspects of our computational implementation of the method.

WOLF ET AL. 5 of 19



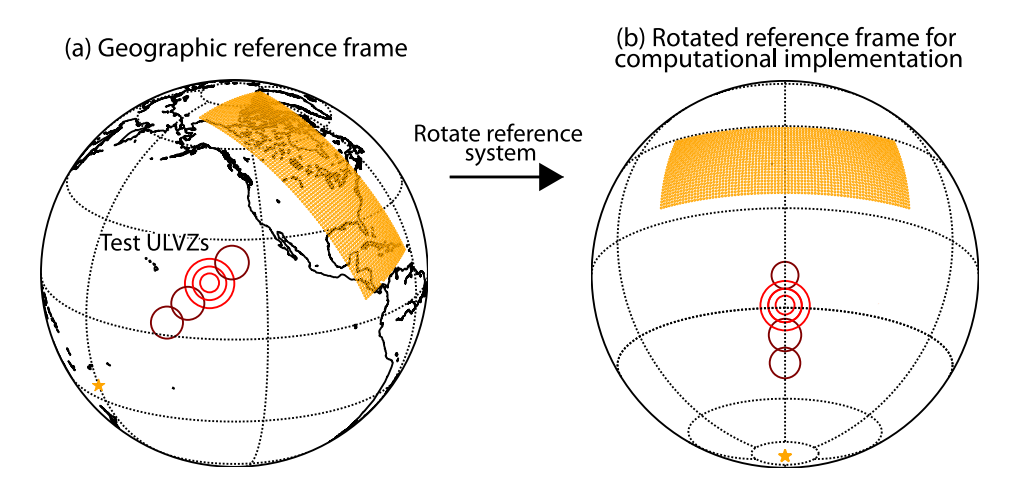


Figure 3. Rotation of reference frame and travel time calculations. (a) Event (yellow star), stations (yellow dots), and ultralow velocity zones used in synthetic tests (dark and light red circles) as implemented in the geographic reference frame. (b) The geographic reference frame is rotated so that the event is positioned at the south pole in the rotated frame. The same symbols as in panel (a) are used.

5.2. CMB Migration Grid

Heterogeneity anywhere along mantle raypaths of S^* can potentially cause seismic wave scattering, resulting in postcursors. However, relative velocity reductions of mantle scatterers are expected to be an order of magnitude smaller than those of ULVZ anomalies, which are the focus of our investigation. Scattering effects away from the CMB are thus neglected, and we devise our search for heterogeneities along a two-dimensional plane at the CMB for strong ULVZ associated heterogeneities. Synthetic tests for waveform effects similar to scattering near source or receiver are shown in Figures S1c and S2 in Supporting Information S1. In the region of CMB sensitivity of S^* , we construct a grid (Figure 2), each grid point of which we assume to be a potential scatterer location. The grid is constructed in 2° longitude and latitude increments in a rotated reference frame, which is sufficiently dense considering that the first Fresnel zone of $10 \text{ s S}_{\text{diff}}$ waves is approximately 1,000 km across (Li et al., 2022). This grid extends to a distance shorter than the ray-theoretical sensitivity (e.g., 45° for an event with focal depth 0 km) to account for the full-wave sensitivity at such shorter distances (e.g., Lai et al., 2022). At the upper distance range, it reaches the maximum distance of ray-theoretical sensitivity. The reason for this is that while full-wave sensitivity may extend further, its effects are typically observable at only a limited number of distant stations. The grid covers the full azimuthal range of the stations but no additional azimuths (as discussed further in Section 2). For our synthetic simulations, this includes relative azimuths to the great circle paths of $\pm 40^\circ$.

5.3. Waveform Processing

We use instrument-deconvolved transverse component displacement seismograms, which we downsample to three samples per second. Transverse component S* amplitudes are typically larger than those of radial components and exhibit less interfering energy, which makes them particularly well-suited for postcursor analysis (e. g., Cottaar & Romanowicz, 2012). Signal-to-noise ratios (SNRs) are calculated via comparison of the maximum absolute S* amplitude to the largest absolute seismogram amplitude in a time window from 70 to 40 s prior to the predicted S* time window (predictions made using the TauP software (Crotwell et al., 1999)). Data with S* SNRs above 3 are retained for our migration experiment. Maximum S* arrivals are normalized to unity; then, all data (with SNRs > 3) are linearly stacked for a certain number of azimuthal intervals (Figure 5, left panels) to determine an average waveform. In a our experiments, the number of azimuthal intervals used is the ceiling of the whole azimuthal range divided by 20. The average waveform is then subtracted from the single station seismograms in the corresponding azimuthal range (Figure 5, right panel). Subtracting the average S* wavefield (e.g., Schwarz, 2019b) results in station-by-station remainder traces that retain boosted wavefield effects caused by heterogeneity. Figure 5b shows the application of this wavefield separation procedure to an event that occurred on 2 February 2012. Because single-station seismograms would plot on top of each other, we show stacks in narrow azimuth ranges instead. In this example, the postcursor signal is difficult to identify before wavefield subtraction (Figure 5b, left panel). However, after subtraction of average waveforms, it becomes distinctly detectable in the

WOLF ET AL. 6 of 19

21699356, 2025, 6, Downloaded from https://agupubs.onlinelibrary.wiley.com/doi/10.1029/2025JB031367 by Ingv. Wiley Online Library on [11/11/2025]. See the Terms and Conditions (https://onlinelibrary.wiley.com/derms/

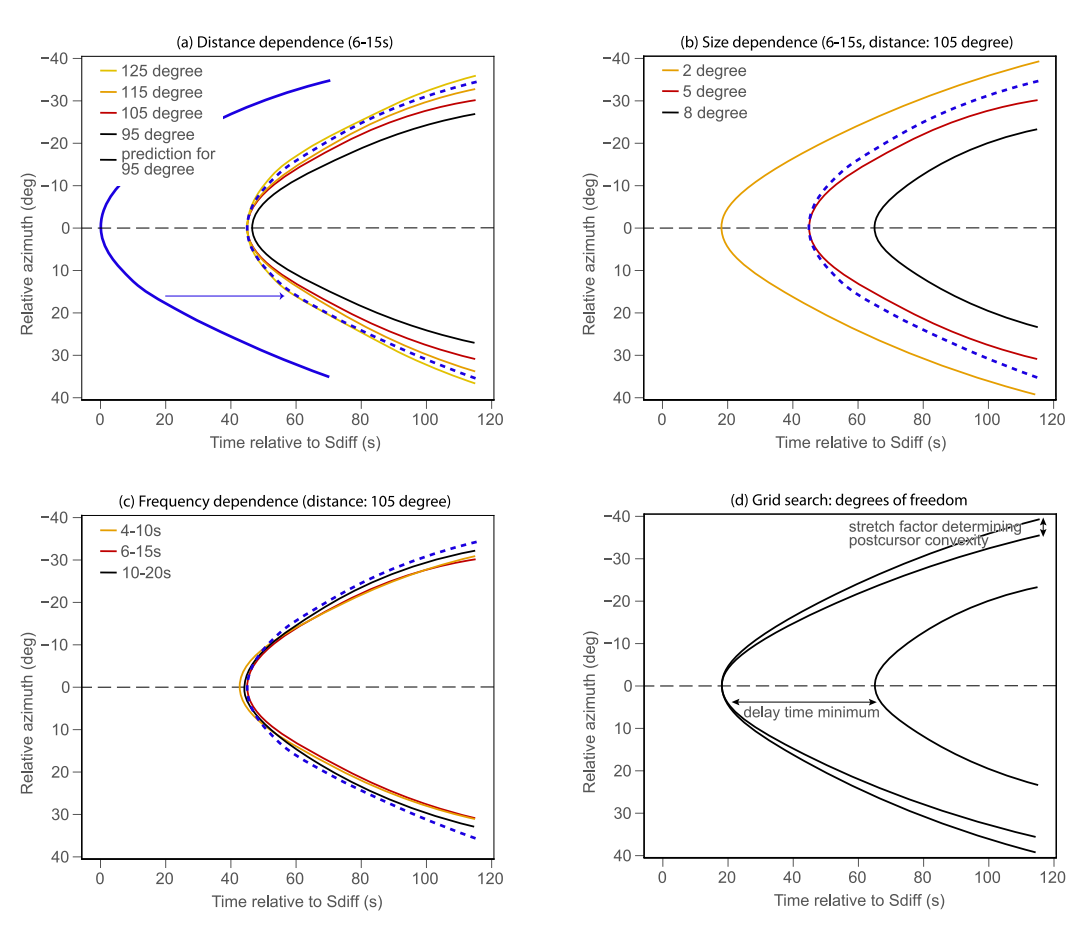


Figure 4. Postcursor arrival time determined from synthetic simulations for a cylindrical ultralow velocity zone (ULVZ) with a radius of 5° , a thickness of 20 km and a velocity reduction relative to PREM of 30%, placed 52° from the source. 0 s time marks the first onset of the S* arrival. (a) Postcursor arrival times after retaining periods between 6 and 15 s for stations at different epicentral source-receiver distances (legend) and different azimuths relative to the ULVZ (y-axis). The predicted arrival for a scatterer at the ULVZ midpoint is shown in blue. This arrival is moved forward in time (dashed blue line) for better comparison of its hyperbolic shape with the arrival times based on synthetic simulations. (b) Same plotting conventions as in panel (a) for different ULVZ sizes. (c) Same plotting conventions as in panel (a) for different bandpass filters (legend). (d) Schematic representation of how postcursor arrival times caused by ULVZs can differ from those predicted by a scatterer. If two degrees of freedom, the minimum delay time relative to $S_{\rm diff}$ and the postcursor convexity are adjusted for the scatterer prediction (e.g., via a grid search), ULVZ postcursors can be approximated.

data (Figure 5b, right panel). In the following, we refer to the waveforms that have undergone the subtraction of the azimuthal averages as "heterogeneity waveforms".

The procedure described in Section 3 yields predicted postcursor travel times relative to the main S* phase for every potential scatterer location defined by the CMB migration grid. We then choose a minimum delay time relative to S* and a stretch factor, which is a multiplier of the delay time (Equation 1), thereby adjusting the postcursor convexity. Using the postcursor delay times derived from these two parameters, we linearly stack the waveforms for each scatterer, aligning them according to the predicted postcursor (traveltime) moveout times. This is schematically presented in Figure 2b for synthetic S* waveforms whose average had not yet been removed. In practice, the stacking is conducted using the heterogeneity waveforms (Figure 5), which mitigates the interference of the main S* phase for relatively small postcursor delay times.

The waveform used in the stack is taken ± 10 s around the predicted scattered energy arrival time. Stacking is only performed for delay times that are within 85 s of the minimum delay time relative to S*. Beyond 85 s, postcursors are often not visible in real seismograms due to the interference of noise. For noise-free synthetics, it is immediately apparent that this procedure will yield high amplitudes whenever signal is stacked (Figure 5a). In the presence of noise where signals of interest are not strong enough to use individual seismograms, seismograms will

WOLF ET AL. 7 of 19

21699356, 2025, 6, Downbaded from https://agupubs.onlinelibrary.wiley.com/doi/10.1029/20251B031367 by Ingv, Wiley Online Library on [11/11/2025]. See the Terms and Conditions (https://onlinelibrary.wiley.com/rems-and-conditions) on Wiley Online Library for rules of use; OA articles are governed by the applicable Creative Commons Licensia

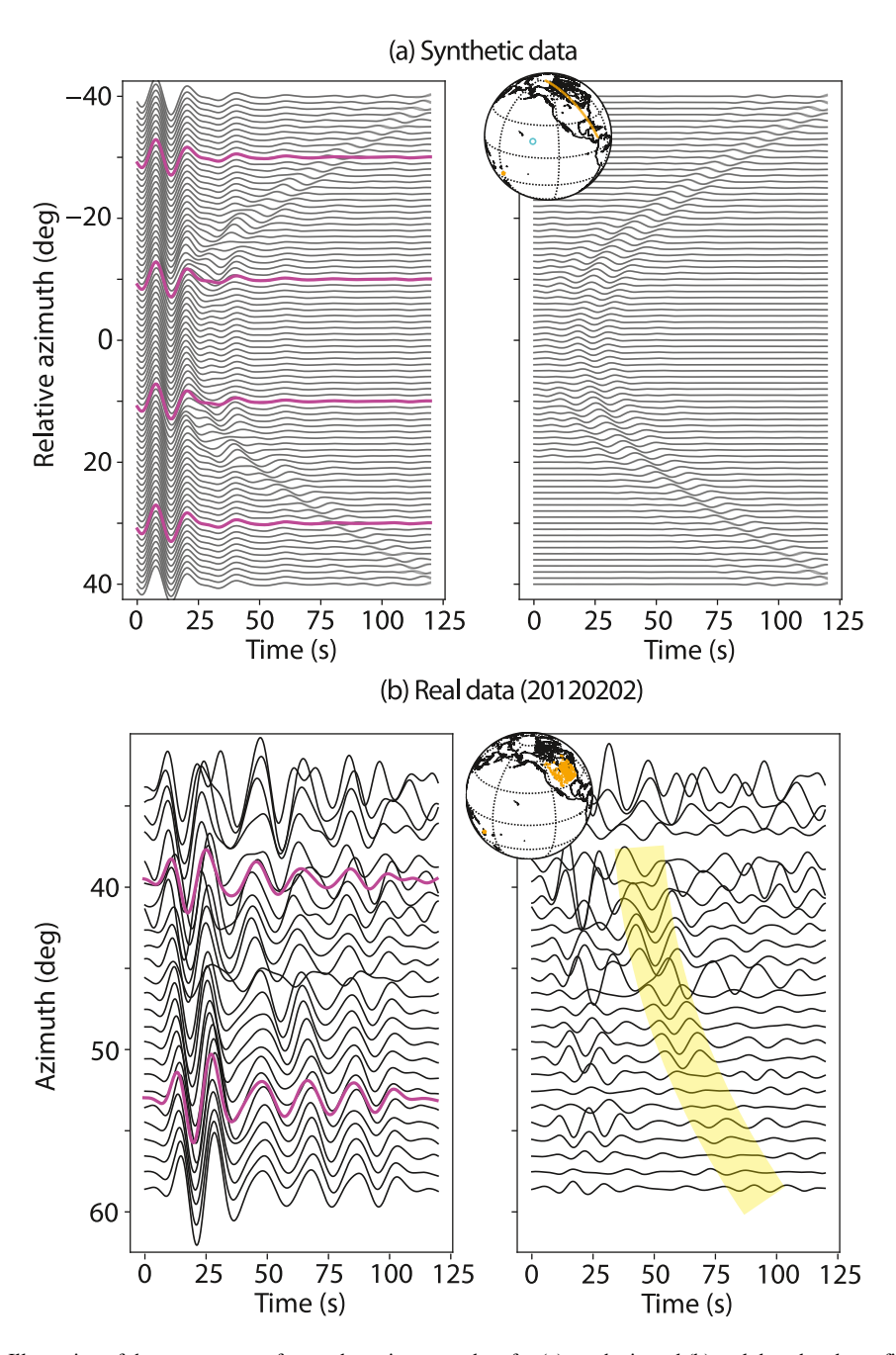


Figure 5. Illustration of the average waveform subtraction procedure for (a) synthetic and (b) real data, bandpass-filtered to retain periods between 10 and 20 s. (a) Left: Transverse displacement waveforms (black) recorded in an epicentral distance of 103° around and after the predicted S* arrival (pulse to the left), calculated for a synthetic input model that includes a ultralow velocity zones (ULVZs). The ULVZ location used for the simulation is marked as a light blue circle (inset; compare to Figure 3). 20° azimuthal waveform stacks are shown in violet. Right: Waveforms after subtraction of the corresponding azimuthal stack. (b) Similar procedure as shown in panel (a) applied to data from an event that occurred 2 February 2012. The inset shows the source (yellow star) and receivers (yellow circles). Left: 1° azimuthal stacks are shown in black and $\sim 15^{\circ}$ azimuthal stacks in violet. Substantial ringing is unlikely to be explained by depth phases due to the shallow source depth (~ 27 km), but could be due to energy trapped in the lithosphere or a complicated source-time function. Right: After subtraction of the azimuthal stacks from the corresponding 1° stacks, a postcursor (yellow) becomes visible.

WOLF ET AL. 8 of 19

only constructively stack if coherent signal is present... Lastly, a scalar is computed by summing the absolute amplitudes of the stack.

We refer to this computed scalar quantity, determined for each grid point, as "heterogeneity energy". If w_{is} (i = 1,2,...,m; s = 1,2,...,n) represent the m 20 s long time windows with a length of n samples that fulfill the criteria described above, used to calculate the signal assuming a certain grid point as a scatterer, the heterogeneity energy H at that grid point can be expressed as:

$$H = \sum_{s=1}^{n} \left| \sum_{i=1}^{m} \frac{w_{is}}{m} \right|. \tag{2}$$

Thus, H is directly proportional to the sum of absolute amplitudes of the stacked waveform for a particular point of the CMB grid. Using positive amplitudes is similar to the approach of previous migration studies (e.g., Kito et al., 2004). This amplitude primarily depends on the properties of the heterogeneity, such as its size and velocity anomaly. Waveforms with the highest postcursor amplitudes compared to the main $S_{\rm diff}$ phase naturally contribute the most to the heterogeneity energy and are recorded at times close to the minimum postcursor delay time relative to S^* . However, these waveforms are insufficient to determine the heterogeneity location (Figure S1 in Supporting Information S1) without the remainder of the quasi-hyperbolic postcursor. We also note that the presence of heterogeneities can influence the amplitude of the main $S_{\rm diff}$ phase at the azimuth at which the heterogeneity is located, which can have an effect of the measured heterogeneity energy. However, if a large enough azimuthal swath is used, this effect will not play a large role for the average.

We repeat this process for minimum delay times relative to S* between 20 and 60 s (in 10 s increments) and stretch factors between 0.7 and 1.3 in increments of 0.2. For this, we utilize PREM-predicted arrival times. Lastly, we select the combination of values that yields the largest heterogeneity energy for any point of the CMB migration grid.

5.4. ULVZ Migration Tests

We first apply our migration procedure to synthetic seismograms, bandpass-filtered between 10 and 20 s, for two isotropic input models that do not possess ULVZ structure. The first model uses the unmodified PREM velocity structure, while the second incorporates a 100 km-thick block with seismic velocities reduced by 3% relative to PREM, as well as sharp edges along the great-circle path. As described earlier, the postcursor field in synthetic seismograms is referenced to S*, and stacks of synthetics are made according to predictions for all CMB grid points across a range of minimum delay times with respect to S* and postcursor convexities. The most coherently stacked combination of values is used and the resultant energy of the stack is then mapped to each CMB grid point. As expected, our tests do not show evidence for CMB heterogeneity for the unmodified PREM model (Figure 6a). On the other hand, sharp velocity contrasts, as present in the second model, can cause S* postcursors (e.g., Ni et al., 2005; To et al., 2005) and therefore, detectable heterogeneity energy (Figure 6a). A slight broadening of a phase due to a moderate velocity contrast as seen in multiple previous studies (e.g., Ni et al., 2005; To et al., 2015) can result in a weaker signal, but is inadequate for determining the heterogeneity location. This is because the broadened pulse fails to stack constructively across a quasi-hyperbolic moveout (Figure S2 in Supporting Information S1).

We then apply our migration algorithm to synthetic data generated for six different ULVZ implementations (Figure 3). The tests demonstrate that the migration algorithm can determine the azimuth along which the ULVZ is located, but does not pinpoint the precise along-great circle path location of the structure (Figure 6b). Additionally, the ULVZ signal is often mapped into a stripe through the middle of the ULVZ, which may be thinner than the lateral extent of the ULVZ. These effects may preclude resolving the precise size of the ULVZ. Additionally, the detectable heterogeneity energy depends on both the size and position of the ULVZ. For example, for a ULVZ that is located far away from the source (e.g., Figure 6b, right panel), the heterogeneity energy will naturally be low at small epicentral distances at which the ULVZ is not (yet) sampled. Similarly, the maximum heterogeneity energy for bigger ULVZs is larger than for smaller structures (if the velocity reduction is the same for both) (Figure 6c). In Figure 6 we adjusted the station distances such that the heterogeneity energy between different test cases is comparable.

WOLF ET AL. 9 of 19



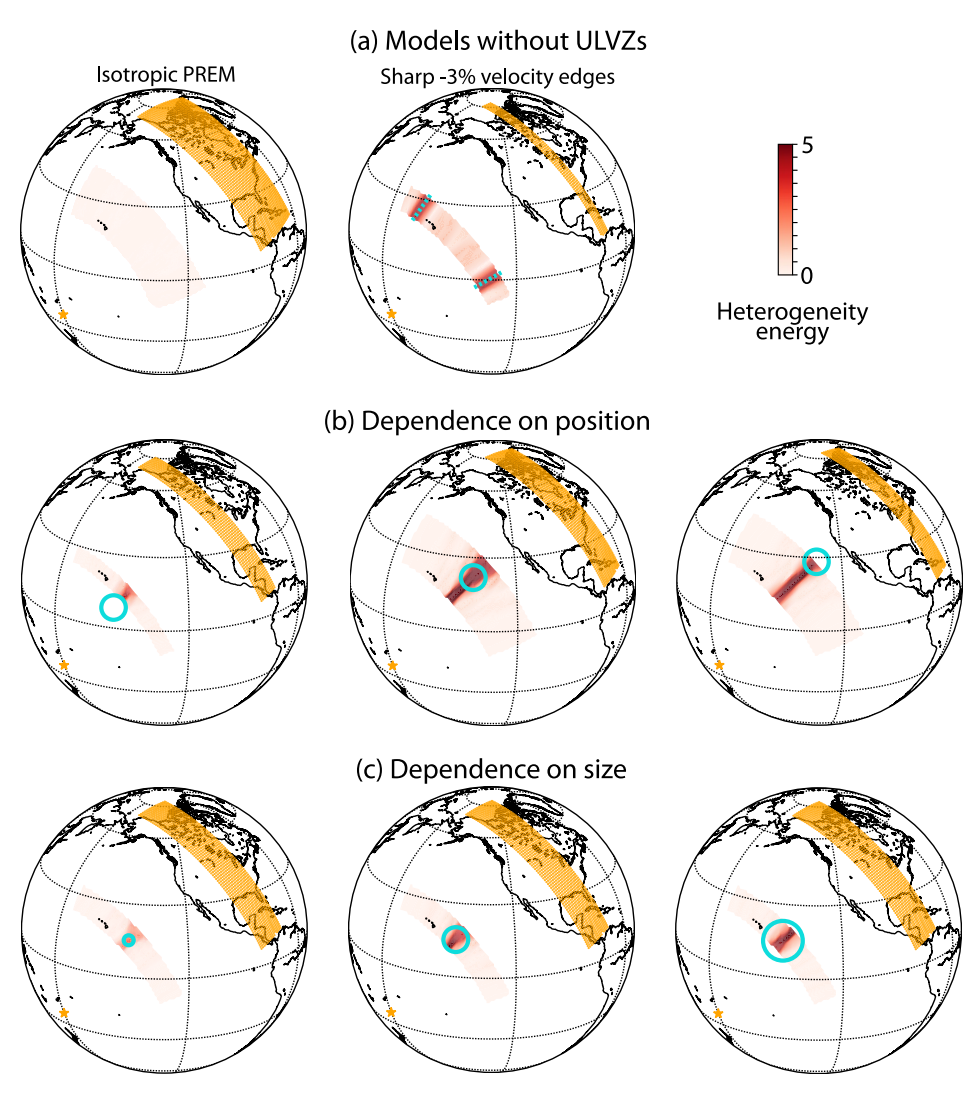


Figure 6. Kirchhoff migration results dependent on the presence (or absence) of different lowermost mantle heterogeneity, calculated from synthetic seismograms. The source location is shown as a yellow star and the stations as yellow circles. Station distances are chosen to lead to a comparable maximum heterogeneity energy (legend; see text) among the different simulations. (a) Results for isotropic PREM (left) and sharp edges (dashed blue lines) with a 3% velocity contrast extending 100 km into the mantle from the core-mantle boundary (right). (b) Dependence on position, which is different in each subpanel. The ultralow velocity zone (ULVZ) incorporated into the simulation is depicted as a light blue circle. (c) Similar to panel (b) but showing results for different ULVZ sizes (blue circles).

We additionally explore how the migration results depend upon different ULVZ shear velocity reductions. These results are displayed in Figure 7. For three different shear velocity reductions (30%, 20%, 10%), the azimuthal location of the ULVZ is accurately recovered, as clear postcursors are produced in all three cases. However, the maximum heterogeneity energy at any grid point is approximately twice as high for the 30% velocity reduction compared to the 10% reduction.

Next, we explore how our migration results are affected by the frequency content of the waveforms, this time using the full range of stations at epicentral distances between 95° and 120° (Figure 8) and a ULVZ located 52° from the source. We use three different bandpass filters, retaining periods from 4 to 10 s (Figures 8a), 6–15 s (Figure 8b), and 10–20 s (Figure 8c). In all cases, the azimuth of the ULVZ is accurately retrieved. Maximum heterogeneity energy is lower for higher frequencies because postcursors have a lower amplitude relative to the main S* phase (Figures 8d–8f). On the other hand, at higher frequencies, the stripe of high heterogeneity energy along the great circle path is thinner, allowing for a more precise localization of the ULVZ center.

WOLF ET AL. 10 of 19

21699356, 2025, 6, Downloaded from https://agupubs.onlinelibrary.wiely.com/doi/10.109290251B031367 by Ingv, Wiley Online Library on [11/11025]. See the Terms and Conditions (https://onlinelibrary.wiely.com/erms-and-conditions) on Wiley Online Library for rules of use; OA articles are governed by the applicable Creative Commons Licensia

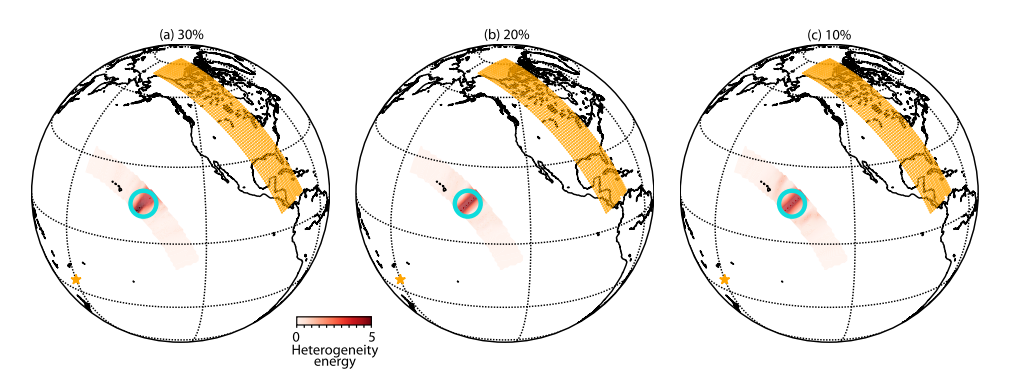


Figure 7. Migration results dependent on ultralow velocity zone (ULVZ) velocity reduction. (a) Heterogeneity energy (legend) for a ULVZ (light blue circle) with a shear velocity reduction of 30% compared to PREM, centered 52° away from the source (black star). The source is shown as a yellow star and the stations as yellow circles (b)–(c) Same as panel (a) for velocity reductions of (b) 20%, and (c) 10%. P wave velocity reductions are one third those of S.

It is also possible to have a slight asymmetry in the two postcursor branches, for example, due to variable velocity structure outside the ULVZ, the ULVZ itself not being cylindrical (as often being assumed) or having a variable height. In this case, the branch that stacks up most coherently will dominate and the ULVZ location can still be recovered (Figure S3 in Supporting Information S1).

For the above synthetic tests, stations were arranged such that ULVZ structures were located along the great circle path of the central azimuth. ULVZ location relative to the central azimuth of some event's station distribution, however, will not be known a priori for real source-receiver configurations. Therefore, we test the ability of our migration technique to resolve ULVZ structure located off the central azimuth great circle path. To accomplish

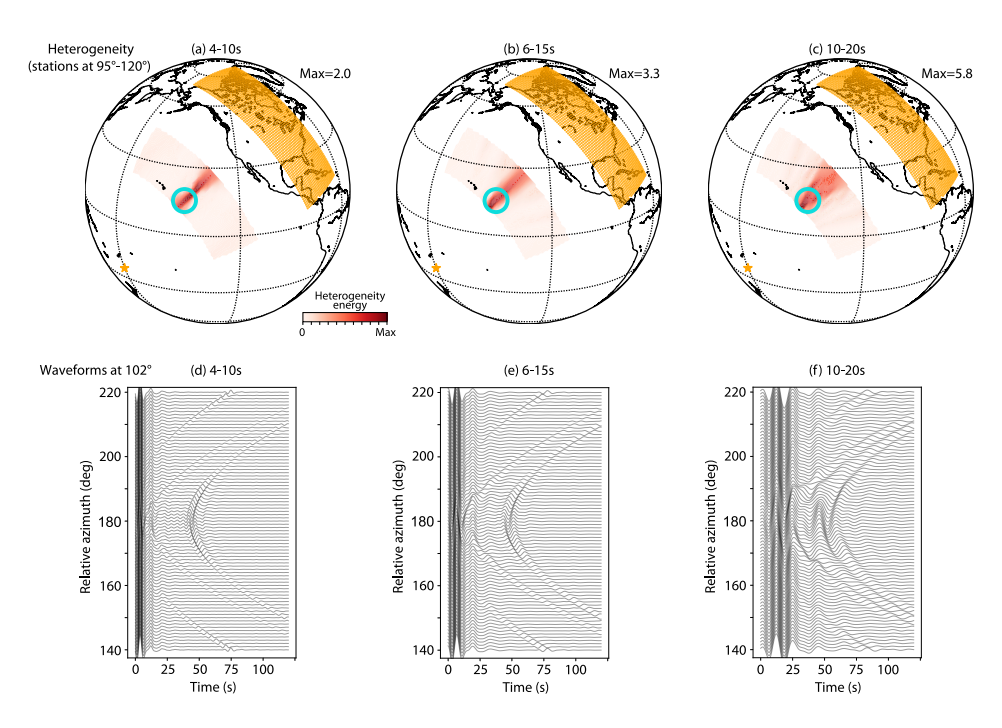


Figure 8. Frequency dependence of Kirchhoff migration results (a)–(c) and postcursor waveforms (d)–(f) for a ultralow velocity zone (light blue circle) with a shear velocity reduction of 30% compared to PREM. (a) Migration results using a bandpass filter retaining periods between 4 and 10 s. The same plotting conventions as in every panel of Figure 6b are used. (b) Same, except using a bandpass filter retaining periods between 6 and 15 s. (c) Same, except using a bandpass filter retaining periods between 10 and 20 s. (d) Synthetic transverse displacement waveforms at an epicentral distance of 102°, used in the migration shown in panel (a), bandpass-filtered to retain periods between 4 and 10 s. (e) Same as panel (d) for data synthetic waveforms used in panel (b), bandpass-filtered to retain periods between 6 and 15 s. (f) Same as panel (d) for data synthetic waveforms used in panel (c), bandpass-filtered to retain periods between 10 and 20 s.

WOLF ET AL.

21699356, 2025, 6, Downloaded from https://agupubs.onlinelibrary.wiley.com/doi/10.1029/2025JB031367 by Ingv, Wiley Online Library on [11/11/2025]. See the Terms and Conditions

ttions) on Wiley Online Library for rules of use; OA articles are governed by the applicable Creative Commons Licenso

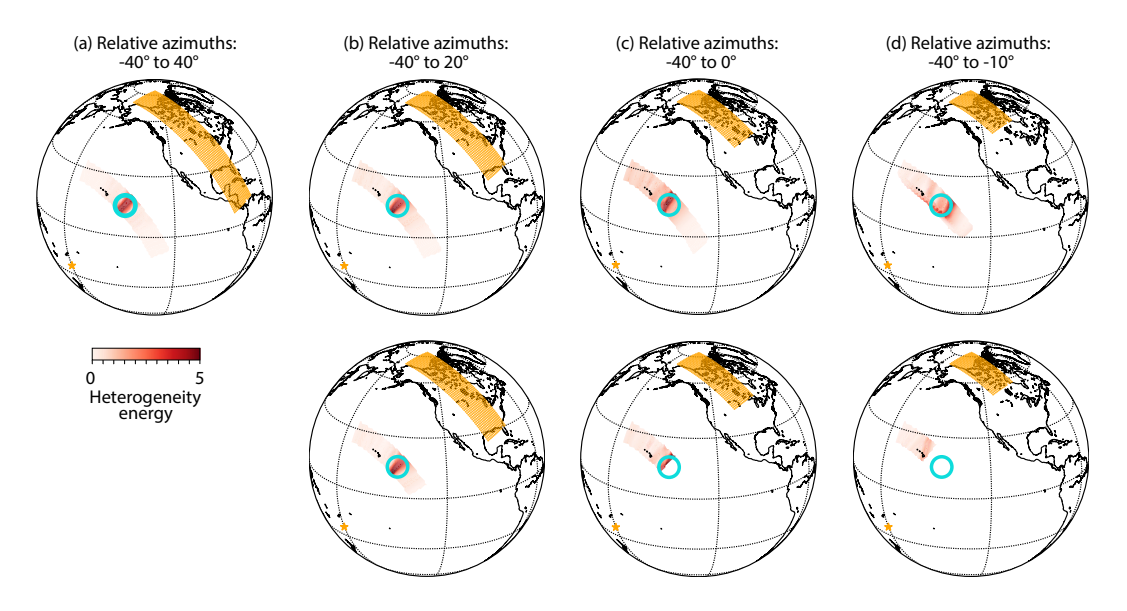


Figure 9. Migration results dependent on the azimuthal receiver distribution. The plotting convention of each subpanel is the same as in each panel of Figure 6b. Stations are placed at a distance range between 95° and 110° , and at relative azimuths with respect to the ultralow velocity zone mid point from (a) -40° to 40° (b) -40° and 20° , (c) -40° and 0° , (d) -40° to -10° . In the top row, we allow the migration algorithm to search for scatterers at relative azimuths between -40° to 40° independent of the azimuthal receiver distribution. Note that for narrow azimuthal receiver distributions some grid points within this range cannot be reached within the maximum allowed time (85 s from the minimum delay time of the postcursor to S*), which is why the heterogeneity grid does not quite reach to relative azimuths of 40° . In the bottom row, scatterer locations are only allowed within the same relative azimuths as the stations.

this, we perform our Kirchhoff migration procedure after progressively removing stations at large azimuths (Figure 9), which effectively shifts the ULVZ off the original great circle path location. ULVZ structure can be resolved well if it is located approximately along the great circle path for at least some of the array stations (Figures 9a–9e), whereas structure away from the great circle path for all stations is not clearly recovered (Figure 9d). Introducing a CMB migration grid that extends beyond the maximum and minimum azimuths can lead to artifacts (Figure 9, upper row). This occurs because the minimum time difference between the postcursor and the main S^* arrival cannot be accurately determined, a limitation also evident when visually inspecting the waveforms. Therefore, we select the azimuthal range of our CMB grid such that it ranges from the lowest to the largest station azimuth (Figure 9, lower row).

Finally, as demonstrated by all these tests, accurately determining the position of a ULVZ along the great-circle path is challenging when its location is sampled from a single azimuth. The same is true if ULVZ structure is analyzed using waveform analysis of S* postcursors without a migration approach unless further processing such as beamforming is used (e.g., Cottaar & Romanowicz, 2012; Li et al., 2022). Therefore, sampling from multiple directions is necessary to determine the location of the ULVZ more precisely. This is demonstrated in Figure 10. As expected, the farther apart different azimuths are from which the ULVZ is covered, the better its location can be determined. Similarly, the denser the ray sampling across multiple azimuths, the better the lateral resolution (Figure 10d). As apparent from Figure 10, our approach maps maximum heterogeneity energies close to the center of the ULVZ, although the structure may be larger. For synthetic data, heterogeneity maps can simply be averaged to determine the ULVZ location, while a weighting procedure dependent on the average noise level proves most effective for real data (Section 6).

6. Real Data Examples

We next apply our Kirchhoff migration approach to real seismic observations, processing the waveforms as described in Section 5.3. For each seismic event, we ensure that at least a 15°-wide azimuthal range is covered after removing traces with low SNRs as low SNRs can lead to spurious signals (Figure S4 in Supporting Information S1). We also guarantee that at least one trace is included every 2° in azimuth. We present three different applications of our migration technique. Data are bandpass-filtered from 6 to 20 s for the first two applications,

WOLF ET AL. 12 of 19

21699356, 2025, 6, Downbaded from https://agupubs.onlinelibrary.wiley.com/doi/10.1029/20251B031367 by Ingy, Wiley Online Library on [11/11/2025]. See the Terms and Conditions (https://onlinelibrary.wiley.com/rems-and-conditions) on Wiley Online Library for rules of use; OA articles are governed by the applicable Creative Commons Licens

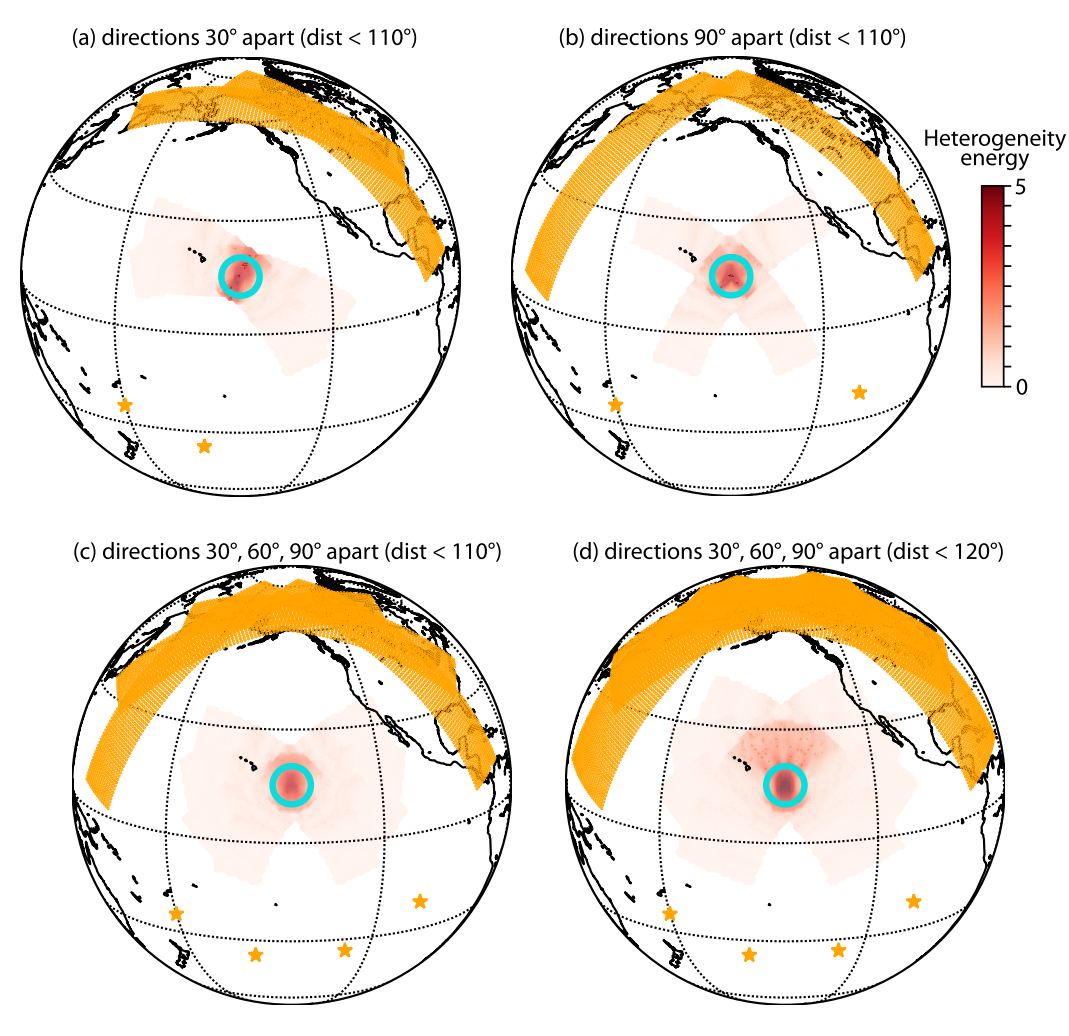


Figure 10. Kirchhoff migration using synthetic data from different seismic events (yellow stars). Stations (yellow circles) are placed at epicentral distances between 95° and 110° (a)–(c) or 95° and 120° (d). (a) Heterogeneity energy (legend) projected to the core-mantle boundary for seismic events that sample the midpoint of the ultralow velocity zone (ULVZ) (light blue) from azimuths that are 30° apart. (b) Same as panel (a) for events that sample the ULVZ midpoint from mutually orthogonal azimuths. (c) Same as panel (a) for four events that sample the ULVZ midpoint from azimuths that are 30°, 60° and 90° apart. (d) Same as panel (e) with seismic stations placed up to 120° epicentral distance.

and 10–20 s for the third example (the Hawaiian ULVZ). Our first two real-data examples show that we can reproduce results inferred from individual seismic events. Then, for the third example, we go one step further and combine results from 28 events with crossing raypaths to obtain a better resolved heterogeneity map (similar to Figure 10).

For our first application, we revisit the 29 July 2011 event, whose event coordinates were used in the synthetic modeling (Section 2; Figure 11a). For this example earthquake, we process data from stations in North America, primarily from the Transportable Array (IRIS Transportable Array, 2003) in the United States, covering the central Pacific Ocean southwest Hawaii and the edge of the Pacific LLVP. This event was previously utilized for ULVZ analysis (Lai et al., 2022; Wolf & Long, 2023), employing computationally expensive forward modeling approaches. The ULVZ suggested by Lai et al. (2022), according to the authors, did not exhibit the hyperbolic S* postcursors that our migration approach benefits from, and we therefore do not expect to resolve it. However, the ULVZ suggested by Wolf and Long (2023) that falls within the azimuthal range of the migration grid, was found based on S* postcursor analyses. We also detect it via our migration approach at the azimuth suggested by Wolf and Long (2023) (Figure 11b). We further compare our results to the ULVZ recently suggested by (Martin et al., 2024), for which there is no evidence for the data from this seismic event (Figure 11a).

WOLF ET AL. 13 of 19

21699556, 2025. 6, Downboaded from https://agupubs.onlinelibrary.wiley.com/doi/10.1029/202518031367 by Ingv, Wiley Online Library on [11/11/2025]. See the Terms and Conditions (https://onlinelibrary.wiley.com/terms-ad-conditions) on Wiley Online Library for rules of use; OA articles are governed by the applicable Creative

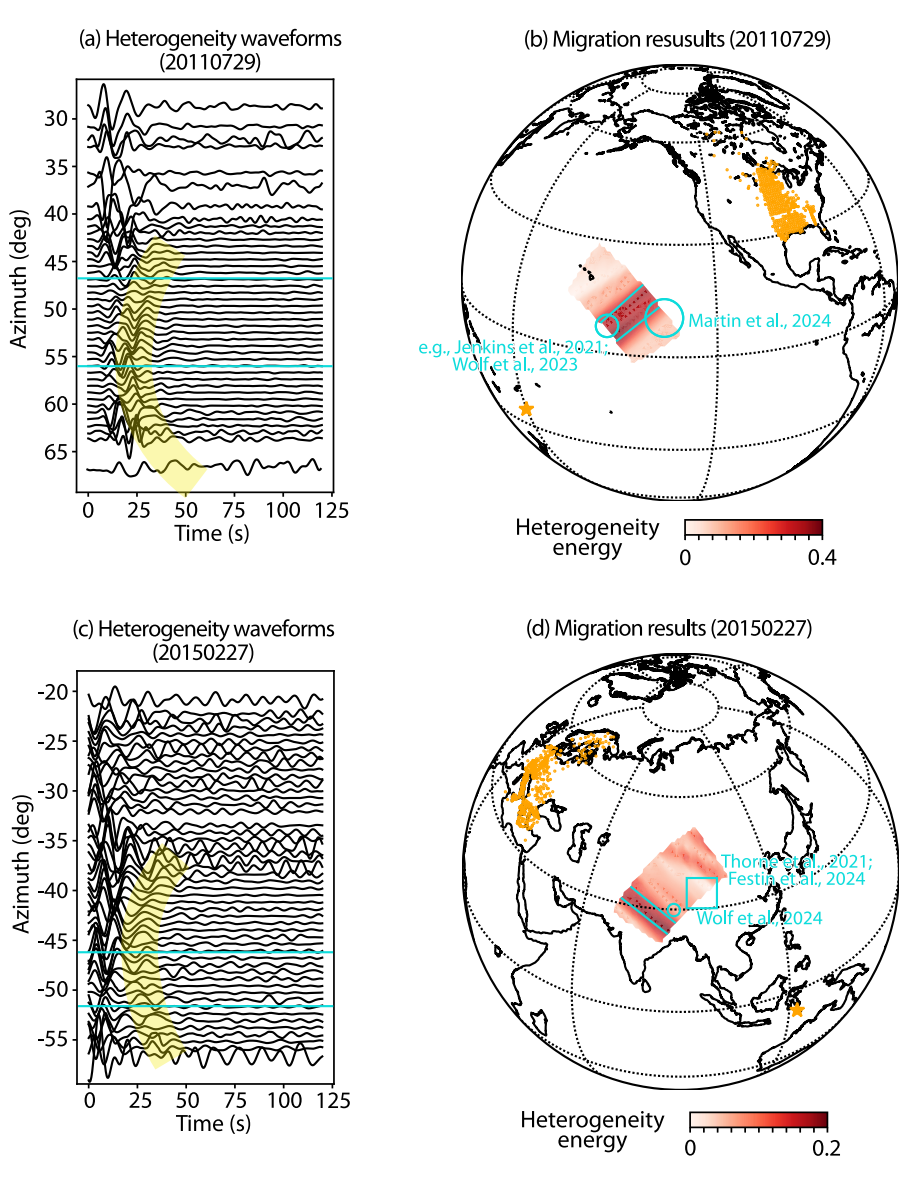


Figure 11. Application of migration technique to real earthquake data from single seismic events. (a) Heterogeneity waveforms for an event from 29 July 2011, recorded across the United States. A postcursor (yellow), which indicates deep mantle heterogeneity, is visible. (b) Migration results for this event. The source is depicted as a yellow star, and stations are represented as yellow circles. Heterogeneity energy (legend) and previously suggested ultralow velocity zone (ULVZ) locations (light blue circles) (Jenkins et al., 2021; Martin et al., 2024; Wolf & Long, 2023) are shown. Cyan lines indicate the azimuth range at which the largest heterogeneity energy is detected. Results support ULVZ locations suggested by Jenkins et al. (2021) and Wolf and Long (2023). No evidence is seen for the ULVZ suggested by (Martin et al., 2024). (c) Same plotting conventions as in panel (a) for an event that occurred on 27 February 2015. (b) Results for heterogeneity beneath central Asia determined from this event. Plotting conventions are as in panel (b). Previously suggested ULVZ locations (light blue circles) are shown. We find evidence for the ULVZ detected by Wolf, Long, and Frost (2024) who also used S*, although their position may be slightly off. ULVZ structure suggested by Thorne et al. (2021) and Festin et al. (2024) using waves other than S* is also nearby, but we do not find evidence for postcursors associated with it.

For the second real data example, we select an event that occurred beneath the Flores Sea on 27 February 2015 (559 km deep). This source-receiver configuration along with the migration results are shown in Figure 11b. This event was used by Wolf, Long, and Frost (2024), who noted a subtle postcursory signal to propose a ULVZ beneath the Himalayas. Additionally, Thorne et al. (2021) and Festin et al. (2024) detected likely ULVZ structure near (but not directly overlapping) this location, using seismic waves other than $S_{\rm diff}$. The heterogeneity waveforms show the same postcursor signal as Wolf, Long, and Frost (2024) (Figure 11a). Our migration approach

WOLF ET AL. 14 of 19



Journal of Geophysical Research: Solid Earth

10.1029/2025JB031367

maps this heterogeneity slightly south of the location suggested by Wolf, Long, and Frost (2024), which appears to be the more likely location based on the heterogeneity waveforms. The ULVZ detected detected by Festin et al. (2024) does not cause a strong S* signal and is not visible in our migration image.

In a third real data application, we apply our migration approach to S* data which, according to Martin et al. (2023), show evidence for the Hawaiian ULVZ. We focus on events that occurred after 1 January 2000, and only use events with moment magnitudes larger than 5.9. We use the quality criteria described in Section 5.3 and discard any events that show azimuthal coverage for less than 15° (after removal of noisy data, see above). This leaves us with a minimum of 66 and a maximum of 493 traces per event. We apply this approach to S* and also to sS* waves if the event depth is deeper than 50 km. We additionally ensure that the S* polarity remains the same for each event along the azimuthal swath used in the analysis. We do this via cross correlation of 3° azimuthal stacks. Figure 12a shows example heterogeneity waveforms for an event that occurred on 9 May 2018, and Figure 12b shows the corresponding migration results. The azimuth at which the Hawaiian ULVZ is located is correctly identified. The somewhat asymmetric migration pattern may indicate secondary seismic scatterers, non-symmetric height, or a non-cylindrical shape of the Hawaiian ULVZ. We combine heterogeneity maps (through linear interpolation onto the same grid) of the real waveforms by weighting them on the average standard deviation of all traces from 60 to 100 s after the predicted S* or sS* arrival. This yields the heterogeneity map shown in Figure 12c which clearly identifies the Hawaiian ULVZ. Separate stripes are visible that combine within the ULVZ (Figure 12c), similar to our test that uses synthetic data (Figure 10).

We note this map only seemingly disagrees with the presence of the ULVZ structures shown in Figure 11a, which are not visible in Figure 12c. As laid out in Section 5.3, our migration approach focuses on the combination of minimum delay time after S* and postcursor convexity that yields the maximum heterogeneity amplitude, which is the Hawaiian ULVZ in the area analyzed in Figure 12c.

7. Discussion

We have implemented a migration algorithm designed to detect heterogeneity at the base of the mantle using postcursors of S* waves. This approach assumes that every point on the CMB within a distance and azimuthal window can scatter waves, and calculates the scattered heterogeneity energy for each point. The migration procedure is an automated data-driven process, and thus minimizes any subjective assessment of whether a signal due to heterogeneity is visible. Our synthetic tests demonstrate that the implemented migration approach is capable of detecting ULVZ structures, although some artifacts in the along-great circle path direction can occur if azimuthal coverage is poor (e.g., Figure 6). This uncertainty can be significantly reduced by by using S* waves from different events that sample structures from different azimuths. In addition to detecting heterogeneity, the migration approach presented here quantifies heterogeneity strength, which effectively measures the strength of the postcursor signal relative to the main S* arrival. The substantial trade-offs that exist between ULVZ height and velocity reduction (Festin et al., 2024; Jenkins et al., 2021; Lai et al., 2022; Russell et al., 2024; Vanacore et al., 2016) are not resolved by our algorithm. Such trade-offs can, however, manifest in the dependence of postcursor characteristics on frequency, and the application of our migration procedure to differently filtered waves is possible (Figure 8).

We have demonstrated our migration approach for three different regions, aiming to determine whether the approach resolves previously mapped ULVZ structures. Our investigation of CMB structure using single seismic events beneath the central Pacific Ocean and beneath central Asia identifies heterogeneity structures that likely correspond to ULVZs detected by Wolf and Long (2023) and Wolf, Long, and Frost (2024). Moreover, we can resolve the location of the Hawaiian ULVZ through sampling from multiple azimuths, confirming the results from previous work (e.g., Cottaar & Romanowicz, 2012; Li et al., 2022; Martin et al., 2023). The ULVZs resolved in the three real-data examples cause postcursors of variable amplitudes due to their different sizes. Our approach is able to identify mega-ULVZs (such as Hawaii), as well as ULVZs which are at the lower end of the detection threshold using S* with a diameter of 200 km (ULVZ beneath central Asia).

The migration approach is versatile in mapping various types of lowest mantle heterogeneity. Migration signals from ULVZs or sharp velocity contrasts can produce similar signals (Figure 6) in case they produce a comparable quasi-hyperbolic moveout. In general, the type of heterogeneity that can be mapped or the minimum heterogeneity energy to be interpreted depends on the noise level of the data. Well-resolved signals result in relatively narrow stripes in the migration image, whereas high-amplitude noise may either stack destructively when

WOLF ET AL. 15 of 19

21699356, 2025, 6, Downloaded from https://agupubs.onlinelibrary.wiley.com/doi/10.1029/2025/B031367 by Ingv, Wiley Online Library on [11/11/2025]. See the Terms and Conditions (https://onlinelibrary.wiley.com/doi/10.1029/2025/B031367 by Ingv, Wiley Online Library on [11/11/2025]. See

and-conditions) on Wiley Online Library for rules of use; OA articles are governed by the applicable Creative Commons Licenses

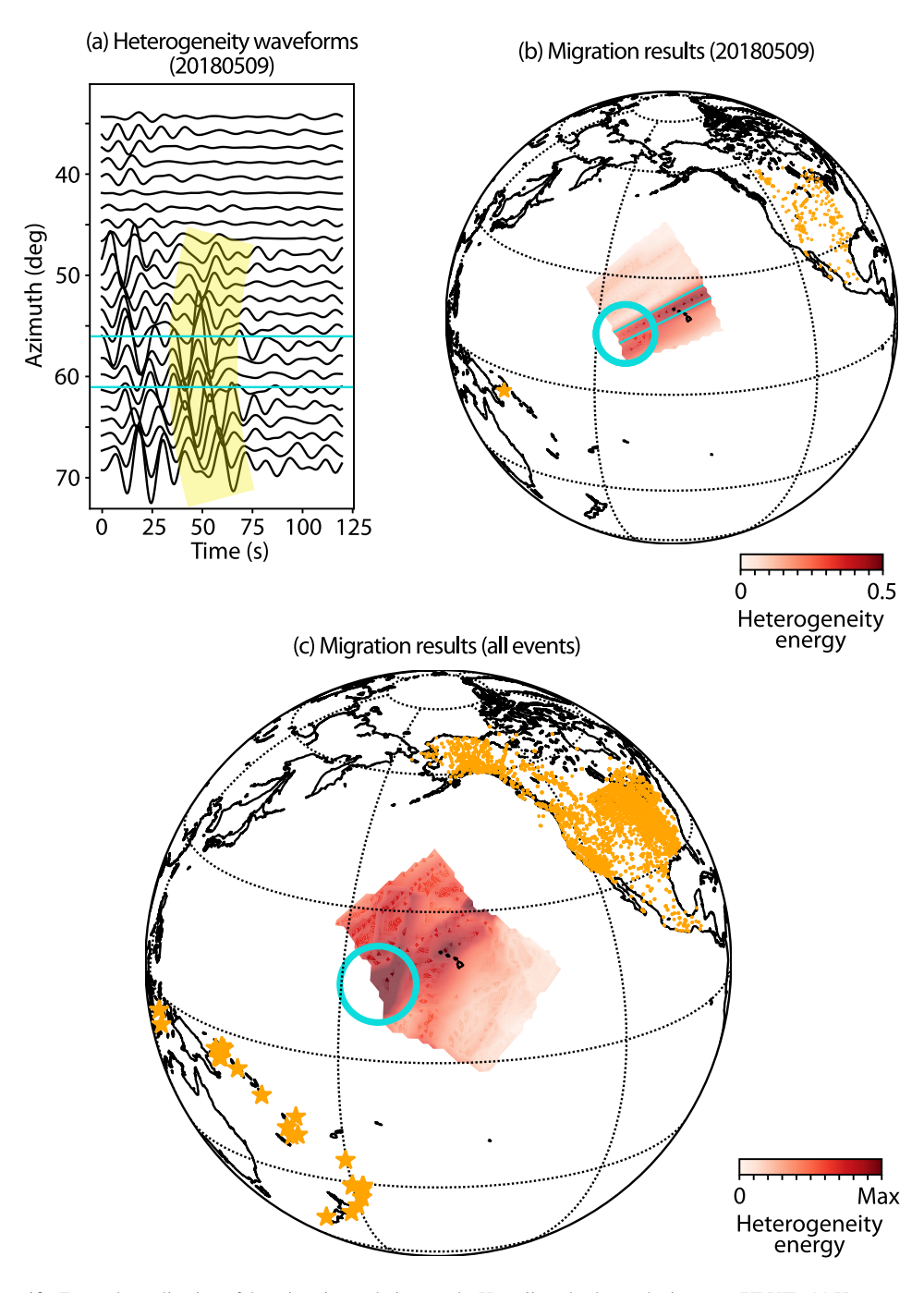


Figure 12. Example application of the migration technique to the Hawaiian ultralow velocity zone (ULVZ). (a) Heterogeneity waveforms as a function of azimuth for an event that occurred on 9 May 2018, in Papua New Guinea and was recorded at stations across North America. Cyan lines indicate the azimuths at which the largest heterogeneity energy is detected. (b) Migration results for this event. Source (yellow star), station (yellow circle) locations and the ULVZ location suggested by (Li et al., 2022) (light blue circle) are shown. Background colors indicate the heterogeneity energy (legend). Cyan lines indicate the azimuths at which the largest heterogeneity energy is detected. (c) Results after combining heterogeneity maps from multiple events using similar plotting conventions as in panel (b). Because heterogeneity maps from individual events are weighted before averaging, magnitudes are not comparable to previous results, which is why the heterogeneity scale does not provide a numeric value for its maximum (Max; legend).

sufficient data are included or produce high heterogeneity amplitudes without clear trends or features (Section 6). By giving an estimate of how well energy stacks for a specific heterogeneity location, the migration approach essentially provides an uncertainty estimate for scatterer locations.

WOLF ET AL. 16 of 19

21699356, 2025, 6, Downloaded from https://agupubs.onlinelibrary.wiley.com/doi/10.1029/2025JB031367 by Ingv, Wiley Online Library on [11/11/2025]. See the Terms and Conditions

conditions) on Wiley Online Library for rules of use; OA

The implemented migration approach is fully automated and can be readily applied to large data sets, enabling the quantification of deep mantle heterogeneity on a large (plausibly global) scale. The implementation in this paper focuses on the largest heterogeneity signal in a particular region, but it can be easily adapted to target specific structures with different sizes, provided they can be described by the minimum postcursor delay relative to S* and the postcursor convexity. Moreover, the algorithm can be applied across the frequency spectrum commonly used for deep mantle heterogeneity studies, allowing it to detect heterogeneity at various scales.

8. Conclusion

We have introduced a new Kirchhoff migration algorithm that utilizes hyperbolic postcursor signals (as a function of azimuth) from S, ScS, and $S_{\rm diff}$ (S*) energy at epicentral distances greater than 95°. Such postcursors are caused by heterogeneity at the base of the mantle. The algorithm provides quantitative assessment of the presence (or absence) of CMB heterogeneity structure, and can be applied to structures with various properties and sizes. Due to challenges to precisely locate heterogeneity along the great circle path, the use of crossing coverage is ideal for determining the precise location of the heterogeneity. Applications of the algorithm to real data produce results consistent with previous studies. The algorithm is fully automated and can be efficiently applied to large data sets to validate proposed ULVZs and search for new ones.

Data Availability Statement

The Generic Mapping Tools (Wessel & Smith, 1998) and ObsPy (Beyreuther et al., 2010) were utilized in this study. Synthetic seismograms were computed using AxiSEM3D (Fernando et al., 2024; Leng et al., 2016, 2019, 2020). For travel time calculations, Pyekfmm (Chen et al., 2023) was employed. All these software are openly available at the links provided in the corresponding publications. All data used in this study are publicly available and were collected and pre-processed as part of ASU's global data collection system for their global data products project. Data were collected from the following on-line data centers: BGR (https://eida.bgr.de/), CNDC (https:// www.earthquakescanada.nrcan.gc.ca/stndon/CNDC/index-en.php), Earthscope (http://service.iris.edu/), ETH (https://eida.ethz.ch/), GEOFON (https://geofon.gfz-potsdam.de/) (GFZ Data Services, 1993), ICGC (https:// www.icgc.cat/en/Ciutada/Explora-Catalunya/Terratremols), INGV (http://cnt.rm.ingv.it/en/webservices_and_ software), IPGP (http://ws.ipgp.fr/) (Institut de physique du globe de Paris and École et Observatoire des Sciences de la Terre de Strasbourg, 1982), KNMI (http://rdsa.knmi.nl/), KOERI (http://www.koeri.boun.edu.tr/new/en), LMU (http://erde.geophysik.uni-muenchen.de/), NCEDC (https://ncedc.org/) (UC Berkeley Seismological Laboratory, 2014), NIEP (https://www.infp.ro/), NOA (http://bbnet.gein.noa.gr/HL/), ORFEUS (http://www. orfeus-eu.org/), RESIF (https://seismology.resif.fr/) (RESIF, 1995), SCEDC (https://scedc.caltech.edu/) (Caltech, 2014), SSN (http://www.ssn.unam.mx/) (Instituto de Geofísica et al., 2024), and TEXNET (http://rtserve. beg.utexas.edu/). All networks and network citations are included as Supporting Information S1-S3, and were derived from the FDSN network code list (https://fdsn.org/networks/).

Acknowledgments

Funding was received by the following sources. JW: Miller Institute for Basic Research in Science at UC Berkeley; EG: partial support from National Science Foundation via Grant EAR-1855624; BS: Fraunhofer Institute for Wind Energy Systems; YL: Yale University; RM: European Union's Horizon 2020 research and innovation program under the Marie Skłodowska-Curie Grant agreement No 858092-IMPROVE; JDW: National Science Foundation via Grant EAR-1853911. We thank Sanne Cottaar and two anonymous reviewers for helpful feedback on both text and methodology.

References

Avants, M., Lay, T., & Garnero, E. J. (2006). A new probe of ULVZ S-wave velocity structure: Array stacking of ScS waveforms. *Geophysical Research Letters*, 33(7), L07314. https://doi.org/10.1029/2005GL024989

Beyreuther, M., Barsch, R., Krischer, L., Megies, T., Behr, Y., & Wassermann, J. (2010). ObsPy: A Python toolbox for seismology [Software]. Seismological Research Letters, 81, 530–533. https://doi.org/10.1111/10.1785/gssrl.81.3.530

Bostock, M. G., & Rondenay, S. (1999). Migration of scattered teleseismic body waves. *Geophysical Journal International*, 137(3), 732–746. https://doi.org/10.1046/j.1365-246x.1999.00813.x

 $Caltech.\ (2014).\ Southern\ California\ earthquake\ center\ [Dataset].\ https://doi.org/10.7909/C3WD3xH1$

Chen, Y., Chen, Y., Fomel, S., Savvaidis, A., Saad, O. M., & Oboué, Y. A. S. I. (2023). Pyekfmm: A Python package for 3D fast-marching-based travel-time calculation and its applications in seismology [Software]. Seismological Research Letters, 94, 2050–2059. https://doi.org/10.1785/0220230042

Cottaar, S., & Romanowicz, B. (2012). An unsually large ULVZ at the base of the mantle near Hawaii. Earth and Planetary Science Letters, 355–356, 213–222. https://doi.org/10.1016/j.epsl.2012.09.005

Crotwell, P., Owens, T. J., & Ritsema, J. (1999). The TauP toolkit: Flexible seismic travel-time and raypath utilities. Seismological Research Letters, 70(2), 154–160. https://doi.org/10.1785/gssrl.70.2.154

Dobrosavljevic, V., Sturhahn, W., & Jackson, J. M. (2019). Evaluating the role of iron-rich (Mg,Fe)O in ultralow velocity zones. *Minerals*, 9(12), 762. https://doi.org/10.3390/min9120762

Dobrosavljevic, V., Zhang, D., Sturhahn, W., Chariton, S., Prakapenka, V., Zhao, J., et al. (2023). Melting and defect transitions in FeO up to pressures of Earth's core-mantle boundary. *Nature Communications*, 14(1), 7336. https://doi.org/10.1038/s41467-023-43154-w

Dziewonski, A. M., & Anderson, D. L. (1981). Preliminary reference Earth model. *Physics of the Earth and Planetary Interiors*, 25(4), 297–356. https://doi.org/10.1016/0031-9201(81)90046-7

WOLF ET AL. 17 of 19

- Dziewonski, A. M., Hager, B. H., & O'Connell, R. J. (1977). Large-scale heterogeneities in the lower mantle. *Journal of Geophysical Research* (1896-1977), 82(2), 239–255. https://doi.org/10.1029/JB082i002p00239
- Etgen, J., Gray, S. H., & Zhang, Y. (2009). An overview of depth imaging in exploration geophysics. Geophysics, 74(6), WCA5–WCA17. https://doi.org/10.1190/1.3223188
- Fernando, B., Wolf, J., Leng, K., Nissen-Meyer, T., Eaton, W., Styczinski, M., et al. (2024). AxiSEM3D An introduction to using the code and its applications. *EarthArXiv*. https://doi.org/10.31223/X5TH7P
- Festin, M. M., Thorne, M. S., & Li, M. (2024). Evidence for ultra-low velocity zone genesis in downwelling subducted slabs at the core–mantle boundary. *The Seismic Record*, 4(2), 111–120. https://doi.org/10.1785/0320240003
- Frost, D. A., Rost, S., Garnero, E. J., & Li, M. (2017). Seismic evidence for Earth's crusty deep mantle. Earth and Planetary Science Letters, 470, 54–63. https://doi.org/10.1016/j.epsl.2017.04.036
- Garnero, E. J., Grand, S. P., & Helmberger, D. V. (1993). Low P-wave velocity at the base of the mantle. *Geophysical Research Letters*, 20(17), 1843–1846. https://doi.org/10.1029/93GL02009
- Garnero, E. J., McNamara, A., & Shim, S.-H. (2016). Continent-sized anomalous zones with low seismic velocity at the base of Earth's mantle. Nature Geoscience, 9(7), 481–489. https://doi.org/10.1038/ngeo2733
- Gazdag, J., & Sguazzero, P. (1984). Migration of seismic data. Proceedings of the IEEE, 72(10), 1302–1315. https://doi.org/10.1109/proc.1984.
- GFZ Data Services. (1993). GEOFON data centre: GEOFON seismic network [Dataset]. https://doi.org/10.14470/TR560404
- Gray, S. H., Etgen, J., Dellinger, J., & Whitmore, D. (2001). Seismic migration problems and solutions. Geophysics, 66(5), 1622–1640. https://doi.org/10.1190/1.1487107
- Hansen, S. E., Garnero, E. J., Li, M., Shim, S.-H., & Rost, S. (2023). Globally distributed subducted materials along the Earth's core-mantle boundary: Implications for ultralow velocity zones. Science Advances, 9(14), eadd4838. https://doi.org/10.1126/sciadv.add4838
- Hedlin, M. A. H., & Shearer, P. M. (2000). An analysis of large-scale variations in small-scale mantle heterogeneity using Global Seismographic Network recordings of precursors to PKP. *Journal of Geophysical Research*, 105(B6), 13655–13673. https://doi.org/10.1029/2000JB900019
- Hutko, A., Lay, T., Garnero, E., & Revenaugh, J. (2006). Seismic detection of folded, subducted lithosphere at the core–mantle boundary. *Nature*, 441(7091), 333–336. https://doi.org/10.1038/nature04757
- Institut de physique du globe de Paris (IPGP)École et Observatoire des Sciences de la Terre de Strasbourg (EOST). (1982). GEOSCOPE, French Global Network of broad band seismic stations [Dataset]. https://doi.org/10.18715/GEOSCOPE.G
- Instituto de Geofísica, Universidad Nacional Autónoma de México, México. (2024). SSN: Servicio Sismológico Nacional [Dataset]. https://doi.org/10.21766/SSNMX/SN/MX
- IRIS Transportable Array. (2003). USArray transportable array. International Federation of Digital Seismograph Networks. Retrieved from https://www.fdsn.org/networks/detail/TA/doi:10.7914/SN/TA
- Jenkins, J., Mousavi, S., Li, Z., & Cottaar, S. (2021). A high-resolution map of Hawaiian ULVZ morphology from ScS phases. Earth and Planetary Science Letters, 563, 116885. https://doi.org/10.1016/j.epsl.2021.116885
- Kito, T., Krüger, F., & Negishi, H. (2004). Seismic heterogeneous structure in the lowermost mantle beneath the southwestern Pacific. *Journal of Geophysical Research*, 109(B9), B09304. https://doi.org/10.1029/2003JB002677
- Lai, V. H., Helmberger, D. V., Dobrosavljevic, V. V., Wu, W., Sun, D., Jackson, J. M., & Gurnis, M. (2022). Strong ULVZ and slab interaction at the northeastern edge of the pacific LLSVP favors plume generation. *Geochemistry, Geophysics, Geosystems*, 23(2), e2021GC010020. https://doi.org/10.1029/2021GC010020
- Landa, E., Shtivelman, V., & Gelchinsky, B. (1987). A method for detection of diffracted waves on common-offset sections. Geophysical Prospecting, 35(4), 359–373. https://doi.org/10.1111/j.1365-2478.1987.tb00823.x
- Lay, T., & Young, C. J. (1996). Imaging scattering structures in the lower mantle by migration of long-period S waves. *Journal of Geophysical Research*, 101(B9), 20023–20040. https://doi.org/10.1029/96JB01887
- Lekic, V., Cottaar, S., Dziewonski, A., & Romanowicz, B. (2012). Cluster analysis of global lower mantle tomography: A new class of structure and implications for chemical heterogeneity. Earth and Planetary Science Letters, 357–358, 68–77. https://doi.org/10.1016/j.epsl.2012.09.014
- Leng, K., Korenaga, J., & Nissen-Meyer, T. (2020). 3-D scattering of elastic waves by small-scale heterogeneities in the Earth's mantle. Geophysical Journal International, 223(1), 502–525. https://doi.org/10.1093/gji/ggaa331
- Leng, K., Nissen-Meyer, T., & van Driel, M. (2016). Efficient global wave propagation adapted to 3-D structural complexity: A pseudospectral/spectral-element approach. *Geophysical Journal International*, 207(3), 1700–1721. https://doi.org/10.1093/gii/ggw363
- Leng, K., Nissen-Meyer, T., van Driel, M., Hosseini, K., & Al-Attar, D. (2019). AxiSEM3D: Broad-band seismic wavefields in 3-D global earth models with undulating discontinuities. *Geophysical Journal International*, 217(3), 2125–2146. https://doi.org/10.1093/gji/ggz092
- Li, Z., Leng, K., Jenkins, J., & Cottaar, S. (2022). Kilometer-scale structure on the core–mantle boundary near Hawaii. *Nature Communications*, 13, 1–8. https://doi.org/10.1038/s41467-022-30502-5
- Luo, Y., Long, M. D., Rondenay, S., Karabinos, P., & Kuiper, Y. D. (2022). Wavefield migration imaging of moho geometry and upper mantle structure beneath southern New England. *Geophysical Research Letters*, 49(13), e2022GL099013. https://doi.org/10.1029/2022GL099013
- Luo, Y., Long, M. D., Rondenay, S., King, S. D., Mazza, S. E., & Wolf, J. (2025). Mantle transition zone-penetrating upwellings beneath the eastern North American margin and beyond. *Journal of Geophysical Research: Solid Earth*, 130(4), e2024JB030005. https://doi.org/10.1029/2024JB030005
- Ma, X., & Thomas, C. (2020). Small-scale scattering heterogeneities in the lowermost mantle from a global analysis of PKP precursors. *Journal of Geophysical Research: Solid Earth*, 125(3), e2019JB018736. https://doi.org/10.1029/2019JB018736
- Martin, C., Bodin, T., & Cottaar, S. (2023). Mapping structures on the core–mantle boundary using sdiff postcursors: Part II. Application to the Hawaiian ULVZ. Geophysical Journal International, 235(3), 2399–2409. https://doi.org/10.1093/gji/ggad345
- Martin, C., Russell, S., & Cottaar, S. (2024). Detection of a ULVZ in the Central Pacific using high frequency Sdiff postcursors. Earth and Planetary Science Letters, 648, 119028. https://doi.org/10.1016/j.epsl.2024.119028
- McNamara, A. K. (2019). A review of large low shear velocity provinces and ultra low velocity zones. *Tectonophysics*, 760, 199–220. https://doi.org/10.1016/j.tecto.2018.04.015
- Ni, S., Helmberger, D. V., & Tromp, J. (2005). Three-dimensional structure of the African superplume from waveform modelling. *Geophysical Journal International*, 161(2), 283–294. https://doi.org/10.1111/j.1365-246X.2005.02508.x
- Niu, F., Silver, P., Nadeau, R., & McEvilly, T. (2004). Migration of seismic scatterers associated with the 1993 Parkfield aseismic transient event. Nature, 426(6966), 544–548. https://doi.org/10.1038/nature02151
- RESIF. (1995). RESIF-RLBP French Broad-band network, RESIF-RAP strong motion network and other seismic stations in metropolitan France [Dataset]. RESIF Réseau Sismologique et géodésique Français. https://doi.org/10.15778/RESIF.FR

WOLF ET AL. 18 of 19



Journal of Geophysical Research: Solid Earth

- 10.1029/2025JB031367
- Rondenay, S. (2009). Upper mantle imaging with array recordings of converted and scattered teleseismic waves. *Surveys in Geophysics*, 30(4–5), 377–405. https://doi.org/10.1007/s10712-009-9071-5
- Russell, S., Irving, J., Myhill, R., & Cottaar, S. (2024). The emerging picture of a complex core-mantle boundary. *Nature Communications*, 15(1), 4569. https://doi.org/10.1038/s41467-024-48939-1
- Schwarz, B. (2019a). Chapter one An introduction to seismic diffraction. In C. Schmelzbach (Ed.), Recent advances in seismology (Vol. 60, pp. 1–64). Elsevier. https://doi.org/10.1016/bs.agph.2019.05.001
- Schwarz, B. (2019b). Coherent wavefield subtraction for diffraction separation. Geophysics, 84(3), V157-V168. https://doi.org/10.1190/geo2018-0368.1
- Seliian, J. A. (1996). Theory, algorithms, and applications of level set methods for propagating interfaces. Acta Numerica, 5, 309–395. https://doi.org/10.1017/S0962492900002671
- Simmons, N. A., & Grand, S. P. (2002). Partial melting in the deepest mantle. Geophysical Research Letters, 29(11), 47-1–47-4. https://doi.org/10.1029/2001GL013716
- Thomas, C., Garnero, E. J., & Lay, T. (2004). High-resolution imaging of lowermost mantle structure under the Cocos plate. *Journal of Geophysical Research*, 109(B8), B08307. https://doi.org/10.1029/2004JB003013
- Thorne, M. S., Leng, K., Pachhai, S., Rost, S., Wicks, J., & Nissen-Meyer, T. (2021). The most parsimonious ultralow-velocity zone distribution from highly anomalous SPdKS waveforms. *Geochemistry, Geophysics, Geosystems*, 22(1), e2020GC009467. https://doi.org/10.1029/2020GC009467
- Thorne, M. S., Takeuchi, N., & Shiomi, K. (2019). Melting at the edge of a slab in the deepest mantle. *Geophysical Research Letters*, 46(14), 8000–8008. https://doi.org/10.1029/2019GL082493
- Tkalčić, H., Young, M., Muir, J., Davies, D. R., & Mattesini, M. (2015). Strong, multi-scale heterogeneity in earth's lowermost mantle. *Scientific Reports*, 5(1), 18416. https://doi.org/10.1038/srep18416
- To, A., Romanowicz, B., Capdeville, Y., & Takeuchi, N. (2005). 3D effects of sharp boundaries at the borders of the African and Pacific superplumes: Observation and modeling. Earth and Planetary Science Letters, 233(1–2), 137–153. https://doi.org/10.1016/j.epsl.2005.01.037
- UC Berkeley Seismological Laboratory. (2014). Northern California Earthquake Data Center [Dataset]. https://doi.org/10.7932/NCEDC
- Vanacore, E., Rost, S., & Thorne, M. (2016). Ultralow-velocity zone geometries resolved by multidimensional waveform modelling. *Geophysical Journal International*, 206(1), 659–674. https://doi.org/10.1093/gji/ggw114
- Wessel, P., & Smith, W. H. F. (1998). New, improved version of generic mapping tools released [Software]. Eos, Transactions American Geophysical Union, 79(47), 579. https://doi.org/10.1029/98EO00426
- Williams, Q., & Garnero, E. J. (1996). Seismic evidence for partial melt at the base of earth's mantle. Science, 273(5281), 1528–1530. https://doi.org/10.1126/science.273.5281.1528
- Wolf, J., Li, M., & Long, M. D. (2024). Low-velocity heterogeneities redistributed by subducted material in the deepest mantle beneath North America. Earth and Planetary Science Letters, 642, 118867. https://doi.org/10.1016/j.epsl.2024.118867
- Wolf, J., & Long, M. D. (2023). Lowermost mantle structure beneath the central Pacific Ocean: Ultralow velocity zones and seismic anisotropy. Geochemistry, Geophysics, Geosystems, 24(6), e2022GC010853. https://doi.org/10.1029/2022GC010853
- Wolf, J., Long, M. D., & Frost, D. A. (2024). Ultralow velocity zone and deep mantle flow beneath the Himalayas linked to subducted slab. *Nature Geoscience*, 17(4), 1–7. https://doi.org/10.1038/s41561-024-01386-5
- Yu, S., & Garnero, E. J. (2018). Ultralow velocity zone locations: A global assessment. *Geochemistry, Geophysics, Geosystems*, 19(2), 396–414. https://doi.org/10.1002/2017GC007281
- Yuan, K., & Romanowicz, B. (2017). Seismic evidence for partial melting at the root of major hot spot plumes. Science, 357(6349), 393–397. https://doi.org/10.1126/science.aan0760
- Zhao, C., Garnero, E. J., McNamara, A. K., Schmerr, N., & Carlson, R. W. (2015). Seismic evidence for a chemically distinct thermochemical reservoir in Earth's deep mantle beneath Hawaii. *Earth and Planetary Science Letters*, 426, 143–153. https://doi.org/10.1016/j.epsl.2015. 06.012

WOLF ET AL.